# FINAL TECHNICAL REPORT: USGS AWARD G22AP00199

Incorporating Rupture Directivity Effects into Probabilistic Seismic Hazard Analyses

**Jeff Bayless**
AECOM
One California Plaza
300 S. Grand Avenue
Los Angeles, 90071, CA, USA
jeff.bayless@aecom.com
916 390 8016

**Norman A Abrahamson**
U.C. Berkeley
760 Davis Hall
Berkeley, CA, 94720 USA

**Paul Somerville**
AECOM
One California Plaza
300 S. Grand Avenue
Los Angeles, CA, 90017 USA
paul.somerville@aecom.com
213 996 2220

Submitted on:
February 8, 2024

*This material is based on work supported by the U.S. Geological Survey (USGS), Department of the Interior, under USGS award number (G22AP00199). The views and conclusions contained in this document are those of the authors and should not be interpreted as representing the opinions or policies of the U.S. Geological Survey. Mention of trade names or commercial products does not constitute their endorsement by the U.S. Geological Survey.*

## Table of Contents

## 1. Abstract

This report describes an update to our 2020 rupture directivity model (Bayless et al., 2020), including formalized instructions for adjustments to the median and aleatory variability of the ground-motion model to which it is applied. Additionally, we provide guidance on implementation, including deterministic and probabilistic applications, and methods for modeling hypocenter locations and multi-segment ruptures. The result is a comprehensive model suitable for use in future probabilistic seismic hazard analyses (PSHAs), including those performed as part of the USGS National Seismic Hazard Model. The model applies to strike-slip earthquakes only. A future update will address directivity effects for other styles of faulting. Implementations of the model in MATLAB (The Mathworks, 2023) and in the open-source hazard software HAZ45.2 (Hale et al., 2018; Abrahamson, 2024) are provided.

# 2. Introduction

The effects of rupture directivity on near-fault ground-motions are known to be significant and should be included to accurately estimate the hazard, especially for long-period ground-motions (Abrahamson, 2000). However, these effects are not explicitly accounted for in typical ground-motions models (GMMs), and therefore not in typical probabilistic seismic hazard analyses (PSHAs) because substantial confusion exists in practice about which directivity models (DMs) to use and how to apply them to the median and aleatory variability of GMMs, especially to complex multi-segment rupture models (Donahue et al., 2019). In the response spectral approach, which we adopt, rupture directivity effects are considered by including adjustment factors to the elastic acceleration response spectrum at 5% damping. This approach lends itself readily to inclusion into PSHA (Rodriguez-Marek and Cofer, 2009).

In this report, we update our rupture directivity model previously developed under USGS Award G18AP00092 (Bayless et al., 2020; Bea20). The directivity model described herein is referred to as Bea24. The directivity model update includes formalized instructions for adjustments to the median and aleatory variability of the GMM to which it is applied. Additionally, we provide guidance on implementation, including deterministic and probabilistic applications, and methods for modeling hypocenters and multi-segment ruptures. The result is a comprehensive model suitable for use in future PSHAs, including those performed as part of the USGS National Seismic Hazard Model. The model applies to strike-slip earthquakes only. Bea24 supersedes our previous models: Bea20, Spudich et al., (2013; BS13), Somerville et al., (1997), and Abrahamson (2000). Model implementations are provided in MATLAB and FORTRAN languages, and the model is implemented in the open-source hazard software HAZ45.2 (Hale et al., 2018; Abrahamson, 2024).

This report addresses the RotD50 (Boore et al., 2010) horizontal component of 5% damped spectral acceleration, which is modeled in the NGA-W2 GMMs. A future update may also address directionality by providing models for the fault-normal and fault-parallel orientations (e.g. Somerville et al., 1997).

## *2.1. Report Contents*

The remainder of this report contains the following sections and appendices:

*Section 3*: Directivity Model Centering: Concepts and Definitions

*Section 4:* Rupture Directivity Adjustment Model

*Section 5:* Model Implementation: Deterministic

*Section 6:* Model Implementation: Probabilistic

*Section 7:* Summary and Conclusions

*Appendix A*: MATLAB and HAZ45 Implementations

*Appendix B:* Calculation of $\overline{f_G}$ (the directivity predictor centering term)

*Appendix C:* Median Model Development

*Appendix D:* Aleatory Variability Model Development

*Appendix E:* Examples

# 3. Directivity Centering

When modeling rupture directivity, the issue of 'centering' has been a longstanding source of confusion in practice. This is because the term has been used in reference to two different concepts:

1. The directivity condition of the mean and standard deviation (of directivity effects) in an existing GMM or GM database. To distinguish from the second concept, this is referred to as '**neutrality**' of the directivity condition hereafter.

2. The directivity condition of a DM used with a non-directive GMM (one which does not explicitly include a term for rupture directivity effects). A '**centered**' DM does not alter the magnitude and distance scaling of the GMM when averaged over uniformly distributed sites at a given rupture distance.

These concepts are discussed further below.

## *3.1. GMM Neutrality vs. DM Centering*

Concept 1: Neutrality of the Directivity Condition

The 'neutrality' refers to the bias of the average directivity condition contained within the empirical data as compared to the average directivity condition for uniformly distributed sites and hypocenters. Any models developed from the empirical data will reflect this bias. Therefore, this concept can apply to a GM database or to an empirical GMM derived from such a database. If the bias is zero, the directivity condition is neutral or 'centered' for future earthquakes. The neutrality issue applies to all GMMs, whether that GMM explicitly accounts for rupture directivity effects or not.

Donahue et al. (2019; D19) evaluated the NGA-W2 GMMs for a neutral average directivity effect by examining the distribution of directivity parameter ΔDPP (Chiou and Youngs, 2014) of the NGA-W2 recordings in magnitude and distance bins. D19 concluded that, on average, the NGA-W2 data reflect a directivity-neutral condition using ΔDPP. Rowshandel (2018) evaluated the neutrality of the NGA-W2 data by comparing distributions of the Rowshandel (2018) directivity parameter with the distributions representing a neutral directivity condition, using all stations with source-site distances less than 25 km.

In this and subsequent sections, we evaluate the neutrality of the mean and standard deviation of the directivity condition of the NGA-W2 GMMs in more detail than D19 and Rowshandel (2018).

The neutrality of the directivity condition is a sampling bias issue. For a given earthquake, the bias will depend on the number of and locations of recording stations, including their distribution of source-site azimuths, and on the finite-fault properties of the rupture, including the rupture geometry and earthquake hypocenter location. For a GM database (consisting of recordings from a large set of earthquakes and recording stations), the neutrality condition depends on the collection of source-site recording pairs and can vary with distance. At a given distance, a database can be biased towards a forward directivity condition (characterized by larger than average long-period ground-motion amplitude with shorter durations), a backwards directivity condition (characterized by smaller than

average long-period ground-motion amplitude with longer durations), or a neutral condition.

As an example, consider a hypothetical ground-motion database consisting of many well-recorded earthquakes, one of which is the vertical strike-slip earthquake shown in Figure 1. In Earthquake #1, all five of the recording stations are at locations where forward directivity effects are expected, and therefore larger than average long-period ground-motion amplitudes are expected for this distance, corresponding to positive total residuals. This is due to their source-site azimuths and distances, and to the hypocenter location, which results in rupture propagation to the north towards the sites. As a result, the ground-motion recordings from Earthquake #1 will have a forward directivity bias. The 1984 Morgan Hill earthquake is an example of a similar situation from the NGA-W2 database (Ancheta et al., 2014; Figure 3-1).

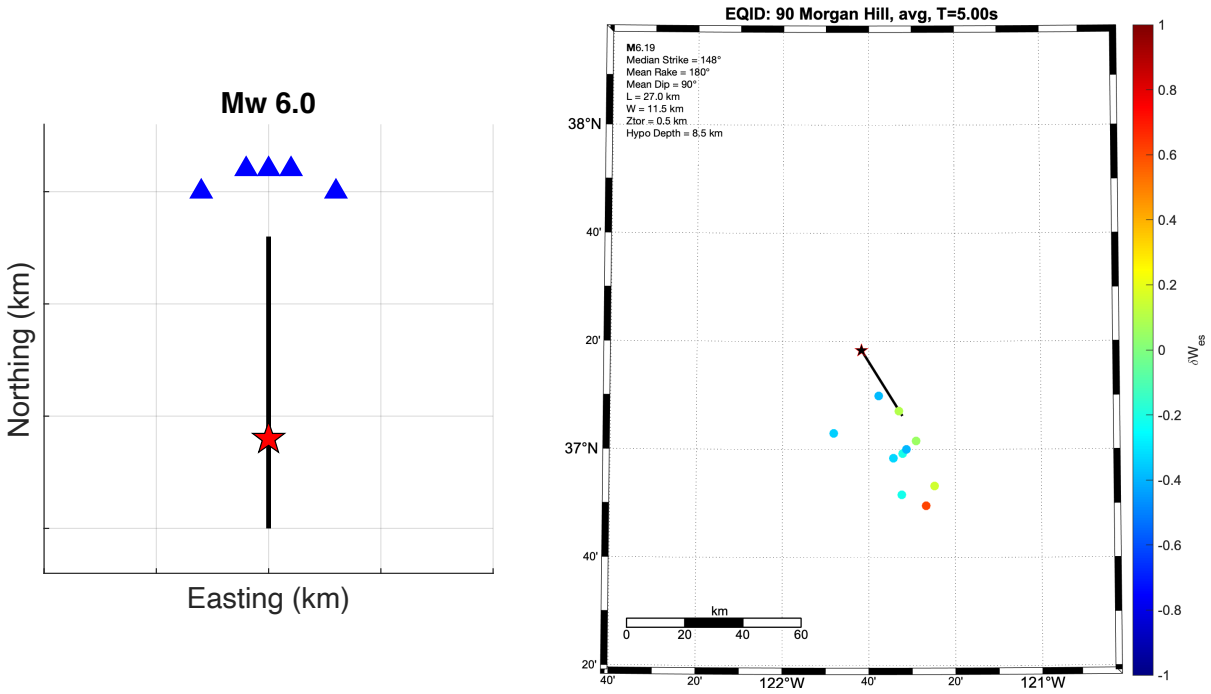


Figure 3-1. Left: Hypothetical Earthquake #1, with fault trace (black), hypocenter (red star), and recording stations (blue triangles) reflecting a directivity condition that is biased toward forward directivity. Right: A map of the 1984 Morgan Hill earthquake trace (black) and recording stations within 50 km with usable period up to 5 sec (circles).

A database made up of only situations like Earthquake #1 would have a strong forward directivity bias. In a database of real earthquakes, the distribution of source-site azimuths will approach a uniform distribution as the sample of earthquakes and recording stations increases; however, the distribution of source-site azimuths may be skewed at a given distance, especially short distances and large magnitudes where recorded databases are still relatively sparse. Additionally, the sampling of the locations of hypocenters in the recorded database with respect to the recording stations may not reflect a directivity neutral condition.

Because of these factors, the neutrality of directivity condition needs to be checked for recorded databases and empirical GMMs. If the bias is zero at a given distance range,

the directivity condition is neutral or 'centered' for that GMM. If the bias is non-zero at a given distance range, the directivity condition in the GMM is also biased. This needs to be checked before a directivity adjustment model can be derived from GMM residuals (and subsequently applied to that GMM), because a directivity model based upon a biased directivity condition will also be biased.

Similar concepts apply to the neutrality condition of the aleatory variability. The range of modeled directivity effects from the distribution of stations in the data set is quantified by their standard deviation of the directivity effects. This standard deviation can be compared with the standard deviation of the directivity effect from uniformly distributed stations with the full range of azimuths to determine if the aleatory variability of the directivity condition is neutral. This method for checking the neutrality of the directivity condition is applied to the NGA-W2 database in Section 3.2

Concept 2: Centering of a Directivity Model

The second concept related to the term 'centering' applies to a DM which is designed to adjust the median and standard deviation of a GMM without directivity. A DM is centered if it does not change the average magnitude and distance scaling of the GMM.

A racetrack is a set of sites uniformly distributed over all azimuths around the finite-fault rupture and with equal source-site distance. For a given earthquake scenario and source-site distance, the mean of the directivity parameter on a racetrack is zero if the DM is centered. When the centered DM is applied to the GMM, the average distance scaling, which does not traditionally vary with azimuth, is unchanged. Similarly, the overall magnitude scaling is unchanged because the mean directivity adjustment over all distances and azimuths for the scenario is also zero.

In other words, a centered DM predicts azimuthally varying median adjustments, but the mean of these is zero at a given distance. This is necessary because the magnitude and distance scaling of the GMM are centered with respect to the recorded data used to develop the GMM. Applying a non-centered DM implies that the magnitude and/or distance scaling of the GMM were biased.

The Chiou and Youngs (2014; CY14) GMM is the only NGA-W2 model to explicitly incorporate directivity effects. CY14 uses the centered directivity predictor $\Delta DPP$. The approach taken by CY14 is to center $\Delta DPP$ on its mean, defined as the mean $DPP$ value over a suite of sites located at the same distance to an earthquake over all azimuths (sites on a racetrack). Because mean $DPP$ is specific to an earthquake, CY14 fit a parametric approximation of mean $DPP$ to each NGA-W2 earthquake. The approach of centering the directivity predictor on its mean is also taken by Rowshandel (2013; Chapter 3 of Spudich et al. 2013) and Rowshandel (2018). Centering of the model described in this report is discussed further below.

Relationship between GMM Neutrality and DM Centering

For any GMM without directivity, the average directivity effect in the observed dataset is implicitly included in the median. The GMM neutrality addresses the reference directivity condition corresponding to that median. The CY14 and Bea20 DMs were developed primarily from NGA-W2 ground-motion data, either as part of the GMM regression (CY14) or from GMM residuals (Bea20). Therefore, these DMs also implicitly include the average

directivity effect in the dataset, to the extent that the models are based on the NGA-W2 data.

However, the centering term of a DM is not necessarily the same as the GMM neutrality term (the average directivity bias). In the case of Bea20, the model was not developed at discrete rupture distances due to data limitations, and instead wide rupture distance ranges were grouped together. The Bea20 model was based on the relationship between residuals and directivity parameters; these parameters include the source-site azimuth and the rupture propagation distance between the hypocenter and the site, but not the rupture distance. This resulted in a model which was centered with respect to the data used to create it, but, in forward application is not centered for any given distance when considering the full range of source-site azimuths.

To address this shortcoming, the Bea24 directivity predictor is centered by removing the centering term at a given rupture distance and for a given scenario. The centering term is the mean of the un-centered directivity predictor over a suite of uniformly distributed sites located at the same distance to an earthquake over all azimuths (sites on a racetrack). The centering of Bea24 is described in Sections 4.2 and in Appendix B.

### *3.2. Neutrality of the NGA-W2 GMMs*

D19 examined the distribution of directivity parameter ΔDPP (Chiou and Youngs, 2014) for NGA-W2 events with **M**>6.5 and sites with $R_{rup}$ < 40 km. For events with at least 10 recordings per earthquake, D19 binned the recordings by distance and found mean ΔDPP values ranging from 0.002 to 0.13. D19 found the mean of all ΔDPP values in the NGA-W2 database, regardless of distance, is 0.011. D19 concluded that, on average, the NGA-W2 data reflect a directivity-neutral condition using ΔDPP.

This section evaluates the neutrality of the mean and standard deviation of the directivity condition of the NGA-W2 GMMs in more detail than D19. In this evaluation, the centered Bea24 and CY14 rupture directivity models are used. The Bea24 model predicts rupture directivity adjustment $f_D$ in natural log units of amplification. At a given rupture distance, the mean of $f_D$ over all source-to-site azimuths is zero because the Bea24 model is centered. This evaluation uses recordings from three NGA-W2 GMMs: Abrahamson et al. (2014), Boore et al. (2014), and Campbell and Bozorgnia (2014). These three GMMs were selected because these GMMs were used to develop the directivity model described in Section 4. Chiou and Youngs (2014) was not included in the model development because it contains directivity adjustments.

The CY14 directivity adjustment (natural log units of amplification) is $f_{DPP}$ and is based on the centered directivity predictor $\Delta DPP$. For the analysis here, Jennifer Donahue (personal communication) provided a spreadsheet of $\Delta DPP$ values calculated by Brian Chiou for each recording in the NGA-W2 database. The $\Delta DPP$ values were converted to $f_{DPP}$ using Equation 7 of CY14, which applies a constant, magnitude taper, distance taper, and period dependence to $\Delta DPP$.

Evaluation Method

We select the set of earthquakes listed in Table 3-1 to evaluate the neutrality of NGA-W2. The earthquakes need to be large enough in magnitude to have a finite-fault model for calculating the CY14 and Bea24 directivity adjustments. Because directivity models are

less established for reverse and normal style of faulting earthquakes, the focus here is on strike-slip and select oblique style of faulting earthquakes. The procedure used to evaluate the neutrality of the directivity condition is:

1) For each earthquake listed in Table 3-1, identify NGA-W2 recordings with $R_{rup}$ < 100 km and which were used by the following GMMs: ASK14, BSSA14, and CB14. At rupture distances larger than 100 km, both the Bea24 and CY14 directivity models have no effect. Calculate $f_D$ and $f_{DPP}$ for these earthquakes and recording locations. Note that the $f_D$ and $f_{DPP}$ are unrelated to GMM residuals. These depend only on the DM and the parameters describing the earthquake sources (rupture geometry, magnitude, hypocenter location) and stations (rupture distance and location of the station with respect to the finite-fault rupture).

2) For each earthquake listed in Table 3-1, calculate $f_D$ on a densely sampled grid of station locations (0.5 km grid spacing). Figure 3-2 shows a map of $f_D$ at T=3 sec for the Landers earthquake at the dense grid of stations (contours; step 2) and at the recording stations (circles; step 1).

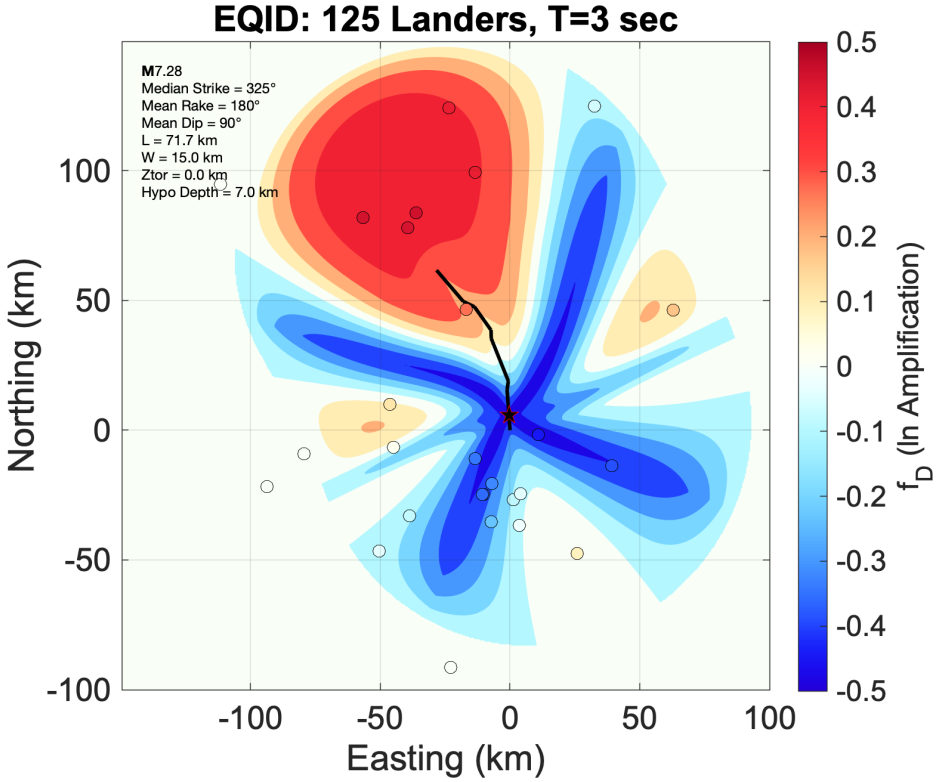


Figure 3-2. A map of the Landers earthquake showing $f_D$ at T=3 sec for at all locations (contours), at the locations with ground-motion recordings (circles), the fault trace (black), and hypocenter (star).

3) For each earthquake listed in Table 3-1, group the NGA-W2 recording stations into rupture distance bins and calculate the sample mean of $f_D$ and $f_{DPP}$ ($\overline{f_D}$ and $\overline{f_{DPP}}$) and sample standard deviations ($s_{fD}$ and $s_{fDPP}$) within each bin. Table 3-1

lists $\overline{f_D}$ and $\overline{f_{DPP}}$ for each earthquake and for two distance bins: $R_{rup}$ less than 20 km and $R_{rup}$ less than 40 km. Evaluate the neutrality of the directivity condition for individual earthquakes.

4) For the complete set of earthquakes listed in Table 3-1, group the gridded stations into rupture distance bins and calculate the population standard deviations ($\sigma_{fD}$) within each bin. The population mean of $f_D$ is equal to zero for the gridded stations because the Bea24 model is centered.

5) Evaluate the neutrality of the directivity condition for the NGA-W2 recordings. For a given rupture distance bin, a completely neutral directivity condition will have $\overline{f_D}$ equal to zero and will have $s_{fD}$ equal to $\sigma_{fD}$. This procedure is repeated for different spectral periods (T).

Evaluation of Individual Earthquakes

The values presented here, including Table 3-1, are for T=3 seconds. The Landers earthquake (Figure 3-2) has $\overline{f_D}$ = -0.018 from four stations within 20 km, and $\overline{f_D}$ = -0.045 from 13 stations within 40 km. These values represent an approximately neutral directivity condition, as expected because of the good azimuthal coverage of the recording stations. Of the 22 events, 14 have $\left|\overline{f_D}\right|$ < 0.1, representing less than about 10% difference from a neutral mean directivity condition for their respective recording station locations.

The Morgan Hill earthquake (Figure 3-1) has $\overline{f_D}$ = 0.247 from 17 stations within 40 km, representing a strong forward-directivity bias. The 2010 Darfield and 1999 Duzce earthquakes were relatively well-recorded and also have strong forward directivity biases ($\overline{f_D}$ = 0.237 and 0.185, respectively) for stations within 40 km. The value $\overline{f_D}$ = 0.247 represents a 28% difference from a neutral mean directivity condition. The Manjiil earthquake has the strongest forward directivity bias; however, this is determined from a single available recording station within 40 km.

The Parkfield and Wenchuan earthquakes have the strongest backward-directivity biases of the events listed in Table 3-1 with $\overline{f_D}$ = -0.045 and -0.046 for stations within 40 km, respectively. These backward-directivity biases, at only a few percent different from neutral, are weaker than the strongest forward-directivity cases (Morgan Hill, Darfield, and Duzce). This is reflected in the mean of $\overline{f_D}$ from all 22 earthquakes, giving equal weight to each earthquake, which is 0.092 (9.6%) for stations within 20 km and 0.076 (7.9%) for stations within 40 km.

Table 3-1. Evaluation the neutrality of the directivity condition of three NGA-W2 GMMs, T=3 sec.

| Earthquake Name | M | NGA-W2 EQID | No. of recordings with $R_{rup}$ < 20 km | $\overline{f_D}$ R < 20 km | No. of recordings with $R_{rup}$ < 40 km | $\overline{f_D}$ R < 40 km |
|---|---|---|---|---|---|---|
| 1979 Coyote Lake | 5.74 | 48 | 7 | -0.018 | 9 | -0.041 |
| 1979 Imperial Valley | 6.53 | 50 | 23 | 0.097 | 31 | 0.109 |
| 1984 Morgan Hill | 6.19 | 90 | 9 | 0.31 | 17 | 0.247 |
| 1986 North Palm Springs | 6.06 | 101 | 7 | 0.072 | 9 | 0.063 |
| 1986 Chalfant Valley | 6.19 | 103 | 3 | -0.006 | 9 | -0.081 |
| 1987 Whittier Narrows | 5.99 | 113 | 18 | 0.011 | 58 | 0.013 |
| 1987 Superstition Hills | 6.54 | 116 | 6 | 0.12 | 8 | 0.092 |
| 1989 Loma Prieta | 6.93 | 118 | 17 | 0.147 | 37 | 0.108 |
| 1992 Landers | 7.28 | 125 | 4 | -0.018 | 13 | -0.045 |
| 1995 Kobe | 6.9 | 129 | 9 | 0.137 | 16 | 0.067 |
| 1999 Kocaeli | 7.35 | 136 | 4 | 0.014 | 6 | -0.015 |
| 1999 Duzce | 7.14 | 138 | 11 | 0.236 | 14 | 0.237 |
| 1990 Manjil | 7.37 | 144 | 1 | 0.365 | 1 | 0.365 |
| 1999 Hector Mine | 7.13 | 158 | 1 | 0.29 | 2 | 0.199 |
| 2002 Denali | 7.9 | 169 | 1 | -0.016 | 1 | -0.016 |
| 2000 Tottori | 6.6 | 176 | 10 | 0.002 | 21 | 0.042 |
| 2003 Bam | 6.5 | 178 | 1 | 0.285 | 1 | 0.285 |
| 2004 Parkfield | 6 | 179 | 54 | -0.059 | 57 | -0.045 |
| 2008 Wenchuan | 7.9 | 277 | 6 | -0.053 | 14 | -0.046 |
| 2010 El Mayor-Cucapah | 7.2 | 280 | 8 | -0.036 | 22 | -0.038 |
| 2010 Darfield | 7 | 281 | 15 | 0.179 | 29 | 0.185 |
| 2011 Christchurch | 6.2 | 346 | 17 | -0.029 | 22 | -0.006 |
| | | | Mean: | 0.092 | Mean: | 0.076 |

Neutrality of the Mean, All Events

Table 3-2 lists results for the 22 earthquakes evaluated by combining all the recording stations from each earthquake into distance bins, for T=3 seconds.

Figure 3-3 shows $\overline{f_D}$ and $\overline{f_{DPP}}$ (sample means of the median directivity effect at the NGA-W2 stations) in distance bins along with their 95% confidence intervals. When the 95% confidence intervals do not overlap zero, the sample means have a statistically significant difference from zero at the 95% confidence level. This figure shows that for most distance bins, the sample means of the median directivity adjustments from both models are not statistically significant from zero, indicating a neutral directivity condition. Exceptions are the distance bins 3-5 km, 10-15 km, and 40-60 km, where there is a small (statistically significant) bias towards the forward-directivity condition. There are no distance bins with a statistically significant bias towards backwards directivity. The Bea24 model has generally larger sample means than the CY14 model.

The bottom of Table 3-2 lists the statistics for distance bins of 0-20 km, 0-40 km, and 0-100 km. All three bins have a small bias towards forward directivity (both models) with the

largest of these for 0-20 km bin ($\overline{f_D}$ = 0.051 ln units; 5.2% increase from neutral). All sites with $R_{rup}$ < 40 km have $\overline{f_D}$ = 0.049 ln units (5.0%), and sites with $R_{rup}$ < 100 km have $\overline{f_D}$ = 0.039 ln units (4.0%).

Table 3-2. Results by distance bin for the 22 earthquakes listed in Table 3-1.

| $R_{rup}$ bin (km) | No. of NGA-W2 stations in distance bin | Sample means and standard deviations; from NGA-W2 stations | | | | Population standard deviation; from gridded stations |
|---|---|---|---|---|---|---|
| | | Bea24: $\overline{f_D}$ (ln) | Bea24: $s_{fD}$ (ln) | CY14: $\overline{f_{DPP}}$ (ln) | CY14: $s_{fDPP}$ (ln) | Bea24: $\sigma_{fD}$ (ln) |
| $0 \le R_{rup} < 1$ | 12 | 0.071 | 0.243 | 0.036 | 0.198 | 0.173 |
| $1 \le R_{rup} < 3$ | 26 | 0.042 | 0.230 | -0.003 | 0.130 | 0.192 |
| $3 \le R_{rup} < 5$ | 29 | 0.098 | 0.190 | 0.023 | 0.091 | 0.209 |
| $5 \le R_{rup} < 10$ | 62 | -0.024 | 0.253 | -0.017 | 0.119 | 0.220 |
| $10 \le R_{rup} < 15$ | 45 | 0.131 | 0.255 | 0.054 | 0.179 | 0.221 |
| $15 \le R_{rup} < 20$ | 58 | 0.047 | 0.210 | 0.010 | 0.182 | 0.219 |
| $20 \le R_{rup} < 30$ | 99 | 0.047 | 0.209 | 0.012 | 0.140 | 0.215 |
| $30 \le R_{rup} < 40$ | 66 | 0.041 | 0.192 | 0.000 | 0.159 | 0.211 |
| $40 \le R_{rup} < 60$ | 110 | 0.056 | 0.183 | 0.005 | 0.117 | 0.189 |
| $60 \le R_{rup} < 80$ | 102 | 0.014 | 0.114 | -0.003 | 0.025 | 0.096 |
| $80 \le R_{rup} < 100$ | 76 | 0.001 | 0.013 | 0.000 | 0.000 | 0.000 |
| | | | | | | |
| $R_{rup} \le 20$ | 232 | 0.051 | 0.237 | 0.013 | 0.153 | 0.216 |
| $R_{rup} \le 40$ | 397 | 0.049 | 0.223 | 0.010 | 0.151 | 0.214 |
| $R_{rup} \le 100$ | 685 | 0.039 | 0.191 | 0.006 | 0.124 | 0.145 |

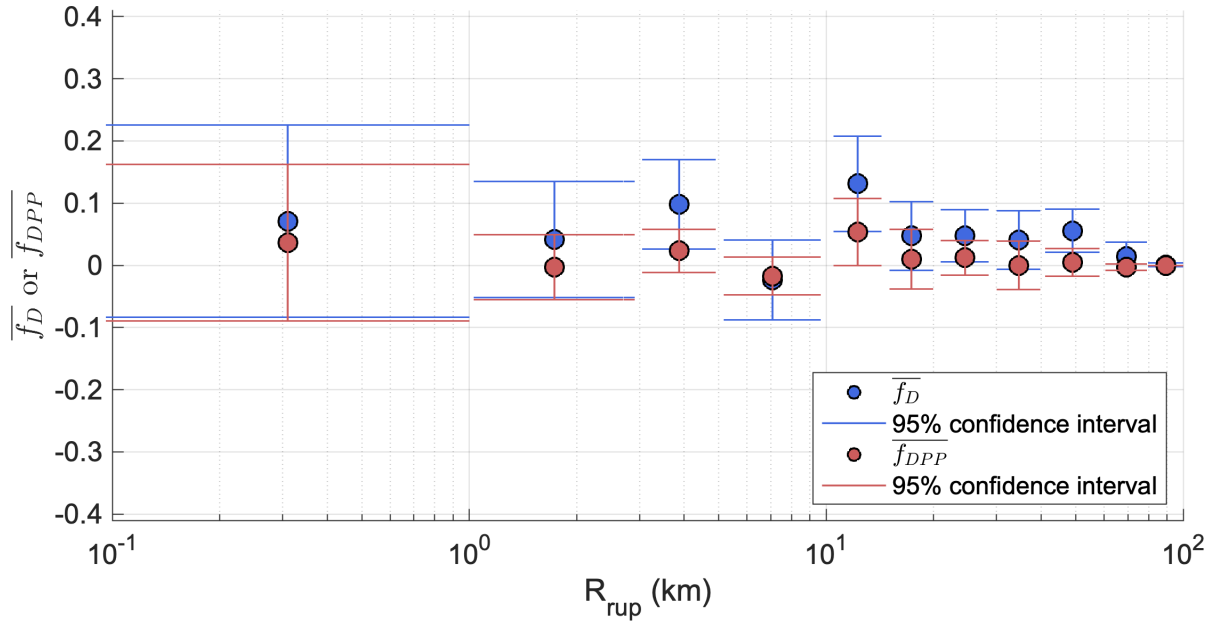


Figure 3-3. Distance bins of $\overline{f_D}$ and $\overline{f_{DPP}}$ (sample means of the directivity effect at the NGA-W2 stations) with their 95% confidence intervals. Confidence interval bar distance widths indicate the extent of the distance bins.

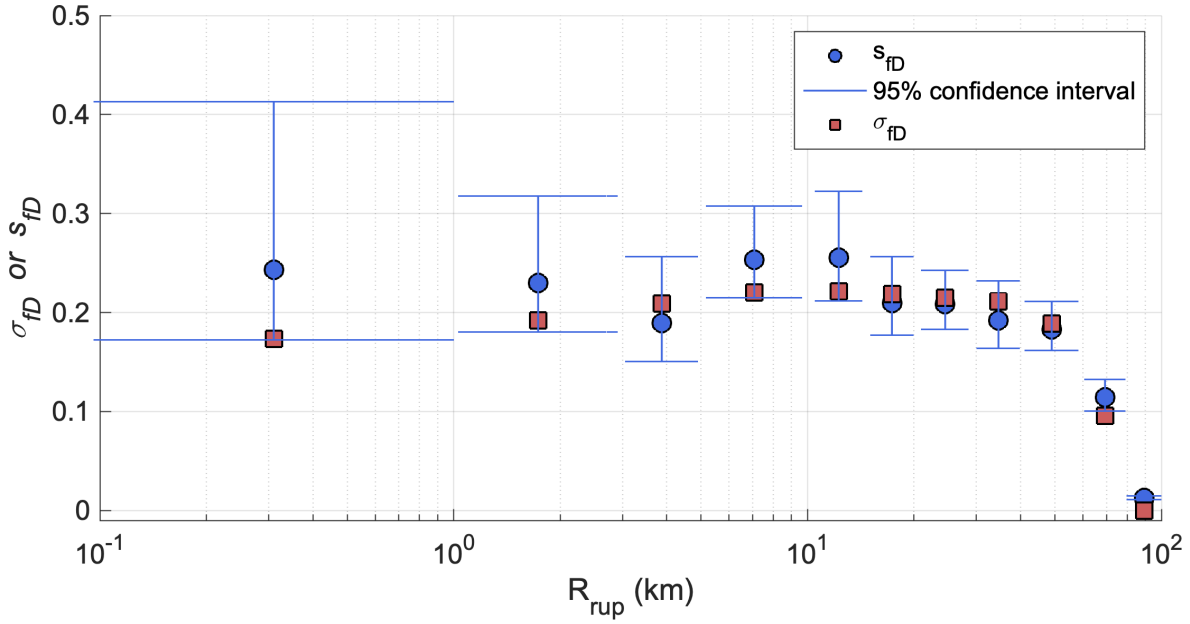


Figure 3-4. Distance bins of $s_{fD}$ (sample standard deviation of the directivity effect at the NGA-W2 stations) with 95% confidence intervals, and $\sigma_{fD}$ (population standard deviation of the directivity effect at the gridded stations). Confidence interval bar distance widths indicate the extent of the distance bins.

Neutrality of the Standard Deviation, All Events

A completely neutral directivity condition for the standard deviation will have $s_{fD}$ (sample standard deviation of the directivity effect at the NGA-W2 stations) equal to $\sigma_{fD}$ (population standard deviation of the directivity effect at the gridded stations).

Figure 3-4 shows $\sigma_{fD}$ and $s_{fD}$ with 95% confidence intervals for T=3 seconds and for the Bea24 model. The CY14 model predictions (based on $\Delta DPP$) were provided only at the NGA-W2 recording stations, not the gridded stations. As a result, Table 3-2 provides the sample standard deviations for CY14, but there is no comparison made for this model.

All distance bins with $R_{rup}$ < 60 km have a population standard deviation contained within the sample standard deviation confidence intervals. At distances shorter than 3 km, where the recorded data is very limited, the confidence intervals are wide and $s_{fD}$ appears biased high. The distance bins with $R_{rup}$ > 60 have a very small positive bias in $s_{fD}$.

Conclusions on Neutrality of NGA-W2

D19 binned the recordings by distance and found mean ΔDPP values ranging from 0.002 ($R_{rup}$ < 40) to 0.13 ($R_{rup}$ < 20), with mean of all ΔDPP values in the NGA-W2 database, regardless of distance, of 0.011. For reference, at 3 seconds period, a value of ΔDPP = 0.01 corresponds to approximately $f_{DPP}$ = 0.002 natural log units of amplification (0.2%), ΔDPP = 0.1 to approximately $f_{DPP}$ = 0.025 ln units (2.5%), and ΔDPP = 1 to approximately $f_{DPP}$ = 0.2 ln units (22%). D19 concluded that, on average, the NGA-W2 data reflect a directivity-neutral condition for the median of ground-motions using ΔDPP.

Table 3-3 summarizes our evaluation of the NGA-W2 directivity condition of the mean using Bea24. At long periods, there is a small bias towards the forward directivity condition. The largest bias, of approximately 6%, is for 10 seconds period and for sites

with $R_{rup} \leq 20$ km. When the distance range for this evaluation is reduced to include sites with $R_{rup} \leq 10$ km, the forward directivity bias is smaller for all spectral periods; this is consistent with the finer distance bins used in Table 3-2 and shown in Figure 3-3, where the $R_{rup}$ = 10-15 km bin has the largest $\overline{f_D}$. The bias towards the forward directivity condition generally decreases with decreasing spectral period. As the distance range of sites to consider is expanded from $R_{rup} \leq 20$ to $R_{rup} \leq 40$ km and $R_{rup} \leq 100$ km, the forward directivity bias also decreases.

For distance bins 3-5 km, 10-15 km, and 40-60 km, there is a small bias (statistically significant at the 95% confidence level) towards the forward-directivity condition. For all other distance bins, the sample means of the directivity adjustments models are not statistically significant from zero, indicating a neutral directivity condition.

In summary, the mean directivity condition of the NGA-W2 recordings (and GMMs derived from them) have a small bias towards forward directivity. That bias varies with distance and spectral period; it is on the order of approximately 5% at long spectral periods and close distances. The forward-directivity bias is smaller at shorter spectral periods and larger distances. To the extent that Bea24 is based on the NGA-W2 recordings, we have assumed that the bias in the mean directivity condition, over all distances and spectral periods, is small enough to ignore.

The standard deviations of the directivity effect at the NGA-W2 recording stations are not inconsistent with the standard deviations of the directivity effect at all possible station locations. Therefore, to the extent that the standard deviation of the NGA-W2 GMM models contain rupture directivity effects, these models can be considered to reflect a directivity-neutral condition of the standard deviation of directivity effects.

As shown in Sections 5 and 6, the Bea24 directivity effect for a specific scenario with a fixed hypocenter can lead to significant (e.g., ±40-50%) long-period changes for a given site. For the same scenario with randomized hypocenter locations, the net effect of modeling directivity in the hazard calculation leads to a relatively small change (e.g., ±5-10%) for a given site and at return periods of 1,000-10,000 years.

Table 3-3. Sample mean of $f_D$ by distance bin and period for the 22 earthquakes listed in Table 3-1.

| **$R_{rup}$ bin (km)** | **T=1 sec** $\overline{f_D}$ (ln) | **T=3 sec** $\overline{f_D}$ (ln) | **T=5 sec** $\overline{f_D}$ (ln) | **T=7.5 sec** $\overline{f_D}$ (ln) | **T=10 sec** $\overline{f_D}$ (ln) |
|---|---|---|---|---|---|
| $R_{rup} \leq 10$ | -0.005 | 0.026 | 0.035 | 0.031 | 0.041 |
| $R_{rup} \leq 20$ | 0.009 | 0.051 | 0.059 | 0.061 | 0.065 |
| $R_{rup} \leq 40$ | 0.013 | 0.049 | 0.058 | 0.054 | 0.055 |
| $R_{rup} \leq 100$ | 0.010 | 0.039 | 0.046 | 0.040 | 0.039 |

# 4. Rupture Directivity Adjustment Model

This section describes the revised rupture directivity adjustment model, Bea24, including components for the median and aleatory variability. This model supersedes previous versions. The model is developed for strike-slip earthquakes only and is based on two datasets: the NGA-W2 (Ancheta et al., 2014) database of recorded ground-motions, and the suite of strike-slip earthquake ground-motion simulations compiled in Bea20. Residual analyses were performed for both datasets independently to inform the rupture directivity modeling. We found that the simulations, which have significantly more near-fault stations and better azimuthal coverage than the data, demonstrate stronger scaling with the directivity parameters and over a broader period range. The NGA-W2 data generally demonstrate weaker scaling over a narrower period range. Accordingly, separate directivity model coefficients are provided for the two datasets. The models derived from both datasets have the same functional form and only differ in their coefficients.

The complete model development process is outlined in Appendices C and D. The remainder of Section 4 describes the model, the required input parameters, constraints and limitations, and identifies the significant changes from Bea20.

## *4.1. Coordinate System*

The model relies on the generalized coordinate system GC2, as formulated by Spudich and Chiou (2015). GC2 defines the strike-normal ($T$) and strike-parallel ($U$) coordinates (in km) of sites located around complex fault geometries, including those which are neither straight nor continuous, e.g. Figure 4-1. Spudich and Chiou (2015) prefer placing the GC2 origin at the first endpoint of the fault trace, so that $U$ along the rupture trace is positive. For our application, we define the origin to be the rupture surface trace ordinate of the up-dip projection of the hypocenter. This is convenient for converting $U$ into our directivity prediction parameter $S$, which is the rupture travel length measured along-strike relative to the hypocenter (described below). With this choice of origin, $S$ is positive in the direction of strike and negative in the anti-strike direction. A MATLAB function for calculating GC2 is provided in Appendix A, and GC2 is implemented in the open-source PSHA software HAZ45 (Hale et al, 2018; Abrahamson, 2024).

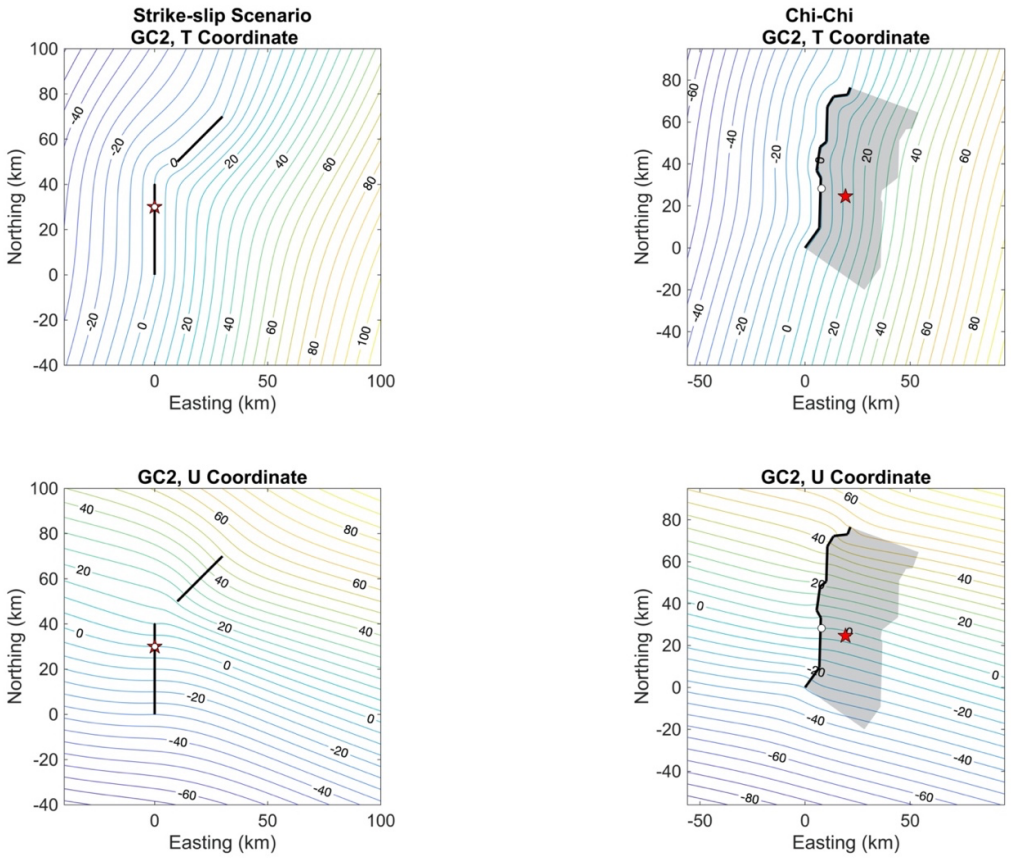


Figure 4-1. Contour maps of GC2 coordinates ($T$, top; $U$, bottom) for (left) a scenario vertically dipping rupture with two disconnected strands with distinct strike angles, and (right) the 1999 Chi-Chi, Taiwan rupture model used in NGA-West2. In both examples the hypocenter location is given by the red star, and the coordinate system origin is given by the white circle.

Note that the fault parallel ordinate, $T$ (km), should not be confused with the spectral acceleration oscillator period, also denoted T (seconds). In this report, we italicize the GC2 ordinate $T$ and provide the units of the oscillator period T (e.g. T=4 sec) whenever possible to avoid confusion.

## *4.2. Median Directivity Adjustment Model*

The median prediction of a non-directive GMM can be adjusted using Equation 1:

$$\ln\big(\, RotD50_{dir}(\boldsymbol{M},\mathrm{T},X)\big) = \ln\big(\, RotD50_{GMM}(\boldsymbol{M},\mathrm{T},X)\big) + f_D(\boldsymbol{M},\mathrm{T},x) \qquad (1)$$

where $RotD50_{dir}$ is the GMM prediction with the directivity adjustment, $RotD50_{GMM}$ is the unmodified GMM-predicted ground-motion, $f_D$ is the median directivity adjustment, $\boldsymbol{M}$ is moment magnitude, T is the oscillator period in seconds, $X$ is the vector of additional GMM explanatory parameters (distance, site parameters, style of faulting, basin parameters, etc.), and $x$ is the vector of parameters describing the position of the site

relative to the rupture. The median directivity adjustment in natural log units, $f_D$, is given by Equation 2:

$$f_D(\boldsymbol{M},\mathrm{T},x) = A(\boldsymbol{M},\mathrm{T})\left(\frac{2}{1+\exp\left[-k\,{f_G}'(\boldsymbol{M},x)\right]}-1\right) \quad (2)$$

in which $k$ is a constant, $A(\boldsymbol{M},\mathrm{T})$ is a magnitude- and period-dependent model parameter, and ${f_G}'(\boldsymbol{M},x)$ is the centered directivity predictor. Equation 2 is a form of the logistic function, which is a family of mathematical models used to describe exponential growth with limiting upper and lower bounds. In Equation 2, the limiting upper and lower bound is $\pm A$, with inflection point at ${f_G}' = 0$. With this functional form, the median directivity adjustment is limited to be $f_D = +A$ when ${f_G}'$ is large and positive (forward directivity) and is limited to $f_D = -A$ when ${f_G}'$ is negative with large absolute value (backward directivity). When the centered directivity predictor is equal to zero ( ${f_G}' = 0$), the median directivity adjustment is also equal to zero ($f_D = 0$). The model parameter $k$ represents the slope of the relationship between ${f_G}'$ and $f_D$. The period-dependence of $f_D$ is incorporated through $A(\boldsymbol{M},\mathrm{T})$, which is modeled with a Gaussian function of period with magnitude-dependent peak period.

Directivity Predictor, $f_G$

The centered directivity predictor is calculated using Equation 3:

$$f_G'(\boldsymbol{M},x) = \left[\, f_G(x) - \overline{f_G(x)} \,\right]\, f_{dist}(\boldsymbol{M},x)\, f_{Ztor}(Ztor) \quad (3)$$

$$f_G(x) = \ln(S_2)\,|\cos(2\theta)| \quad (3a)$$

$$S_2 = \sqrt{9 + (S\cos(Rake))^2} \quad (3b)$$

$$\theta = \left|\tan^{-1}\frac{T}{U}\right|;\ if\ T = U = 0;\ \theta = 0 \quad (3c)$$

where $f_G(x)$ is the Bea20 geometric directivity predictor, $\overline{f_G(x)}$ is the centering term, $f_{dist}$ is the magnitude-dependent distance taper, and $f_{Ztor}$ is the depth-to-top of rupture ($Ztor$) taper. The Bea20 geometric predictor function combines the distance the rupture has traveled toward the site ($S_2$; with minimum value of 3 km so that ln($S_2$) is always greater than one), with the azimuthal predictor function in Equation 3a. The functions $f_G(x)$ and $\overline{f_G(x)}$ are period-independent and only depend on the source-site geometry. For notational brevity, their dependencies on $x$ are suppressed hereafter.

Equation 3b requires the rupture representative rake angle and the parameter $S$, which is readily obtained from the GC2 ordinate $U$. Because we choose the GC2 origin to be the

rupture surface trace ordinate of the up-dip projection of the hypocenter, $S$ is equal to $U$ for sites within the along-strike extent of the rupture (for simple ruptures, the along-strike extent is the rupture length). For sites outside the rupture length (i.e. for sites with nonzero $R_{y0}$), $S$ is equal to the $U$ ordinate of the nearest rupture trace endpoint. Examples of this conversion are given in Bea20.

In Equation 3, the directivity predictor is centered by removing the centering term at a given rupture distance, $\overline{f_G}$, defined as the mean $f_G$ value over a suite of sites located at the same distance to an earthquake over all azimuths (sites uniformly distributed on a racetrack). There is no simple analytical solution for $\overline{f_G}$, so a numerical evaluation is performed; Appendix B documents this procedure and the software in Appendix A provide example implementations. The value of $\overline{f_G}$ is specific to a scenario with given hypocenter location, rupture dimensions, and rupture distance.

The rupture distances ($R_{rup}$) and $Ztor$ tapers are applied to the centered directivity predictor in Equation 3. These reduce the directivity adjustment to zero at $Ztor$ = 20 km and at $R_{rup} = R_{max}$, where $R_{max}$ = 60 km for $\boldsymbol{M}$ 6 and $R_{max}$ = 80 km for $\boldsymbol{M}$ 7 and larger:

$$f_{Ztor}(Ztor) = \begin{cases} 1 - Ztor/20 & For\ Ztor < 20\ km \\ 0 & For\ Ztor \geq 20\ km \end{cases} \quad (3d)$$

$$f_{dist}(\boldsymbol{M}) = \begin{cases} 1 - \exp\left(\dfrac{-4R_{max}(\boldsymbol{M})}{R_{rup}} + 4\right) & For\ R_{rup} \leq R_{max}(\boldsymbol{M}) \\ 0 & For\ R_{rup} > R_{max}(\boldsymbol{M}) \end{cases} \quad (3e)$$

$$R_{max}(\boldsymbol{M}) = \begin{cases} 20\boldsymbol{M} - 60 & For\ 6 \leq \boldsymbol{M} < 7 \\ 80 & For\ \boldsymbol{M} \geq 7 \end{cases} \quad (3f)$$

Logistic Function Parameters

The logistic function in Equation 2 has a constant slope parameter, $k$, and limiting amplitude function, $A(\boldsymbol{M},\mathrm{T})$. The $A(\boldsymbol{M},\mathrm{T})$ is modeled with a Gaussian function of period (Equation 4). This function has maximum value $A_{max}$ and is centered on period $\mathrm{T}_{peak}$. The standard deviation (width parameter) of the Gaussian function is $\sigma_g$. Values for the constants $k$, $A_{max}$ and $\sigma_g$ are listed in Table 4-2. The magnitude dependence of the peak period is modeled with Equation 4a.

$$A(\boldsymbol{M},\mathrm{T}) = A_{max} \exp\left(\frac{(\log_{10}\frac{\mathrm{T}}{\mathrm{T}_{peak}(\boldsymbol{M})})^2}{-2{\sigma_g}^2}\right) \quad (4)$$

$$\mathrm{T}_{\mathrm{peak}}(\boldsymbol{M}) = 10^{-2.15+0.404\boldsymbol{M}} \quad (4a)$$

Model Coefficients

Table 4-1 lists the model functions, model parameters (values used by the functions), arguments (values used to calculate the parameters), and coefficients with a description of each.

The model coefficients are listed in Table 4-2. Two models are developed as described further below; Model 1 is derived from earthquake ground-motion simulations described in Bea20 and Model 2 is derived from the NGA-W2 ground-motion database.

Table 4-1. Description of model functions, parameters, arguments, and coefficients.

| | Name | Description |
|---|---|---|
| **Functions** | $f_D$ | Median directivity adjustment (ln units). |
| | $f_G$, $\overline{f_G}$, $f_G$' | Period independent geometric directivity predictor (uncentered), centering term, and centered directivity predictor |
| | $A$ | Period-dependent lower and upper bound of the directivity adjustment. |
| | $f_{Ztor}$ | Depth to top of rupture taper function. |
| | $f_{dist}$ | Distance taper function. |
| | $\varphi_{Red}$ | Within-event standard deviation reduction. |
| **Parameters** | $S$ | The horizontal length of the rupture traveled between the site and the origin (km). |
| | $S_2$ | Generalized rupture travel distance parameter which accounts for $S$ and the rupture representative rake angle (km). |
| | $\theta$ | The angle made between the average fault strike direction and the vector from the origin to the site (calculated in plan view). |
| | $\mathrm{T}_{peak}$ | The peak period of the directivity effect (sec). |
| | $R_{rup}, R_{max}$ | Distance parameters used in the distance taper function (km). |
| **Arguments** | $U, T$ | The GC2 strike-parallel and strike-normal coordinates relative to the origin, which is defined as the projection of the hypocenter up-dip to the ground surface (km). |
| | Rupture Information | The basic information about the rupture: **M**, segment coordinates, segment lengths, segment strike angles, depth to top of rupture, representative rake angle, and primary hypocenter location. |
| | T | The oscillator spectral period in sec (note the spectral period T is not italicized and care should be taken not to confuse T with the GC2 strike-normal coordinate, $T$). |
| **Coefficients** | $A_{max}$ | The limiting lower and upper bound of the median directivity adjustment. |
| | $k$ | The logistic function slope parameter. |
| | $\sigma_g$ | The standard deviation (width parameter) of the Gaussian function used to model the narrowband formulation. |
| | $e_1$ | Aleatory variability model coefficient. |

Table 4-2. Median model coefficients.

| Coefficient | Model 1 (Simulations) | Model 2 (NGA-W2) |
|---|---|---|
| $\boldsymbol{A_{max}}$ | 0.54 | 0.34 |
| $\boldsymbol{k}$ | 1.58 | 1.58 |
| $\boldsymbol{\sigma_g}$ | 0.38 | 0.26 |

### *4.3. Aleatory Variability Adjustment Model*

The GMM between-event and within-event residuals are well-represented as zero-mean, independent, normally distributed random variables with standard deviations $\tau$ and $\phi$ (Al Atik et al., 2010). The total standard deviation in natural log units, $\sigma$, is given by Equation 5.

$$\sigma = \sqrt{\tau^2 + \phi^2} \tag{5}$$

The subscript GMM is used for the published GMM between-event and within-event aleatory variability ($\tau_{GMM}$ and $\phi_{GMM}$, respectively).

At any site $i$, there are two components of the total within-event variability ($\phi_i$) associated with adding a directivity model in PSHA. $\phi_{Reduction}$ is the reduction of the GMM variability due to improvements in the median prediction. It is the reduction in variability caused by including the directivity term in GMM regression. The second component, $\phi_{i|UH}$, is the added aleatory variability due to the unknown hypocenter (UH) location for a future earthquake. $\phi_{i|UH}$ results from the range of additional ground-motion predictions introduced by integrating over multiple hypocenter locations, each with a different directivity adjustment, in the PSHA. The $\phi_{i|UH}$ is called "parametric aleatory" variability because it is due to an additional physical behavior modeled in the GMM that is not part of the source characterization used in the hazard integral (Liou and Abrahamson, 2024). The relationship between the standard deviation terms is discussed further in Section 6.

The models provided in this section are for standard deviation reductions ($\phi_{Reduction}$) because they are directly calculated from the reduction in the square root of the variance of the within-event residuals resulting from including the median Bea24 adjustment model. To apply the aleatory variability adjustment, a difference in variances should be taken using Equation 6:

$$\phi_{i,Dir}^2 = \phi_{GMM}^2 - \phi_{Reduction}^2 + \phi_{i|UH}^2 \tag{6}$$

in which $\phi_{i,Dir}$ directivity-adjusted within-event variability at site $i$, $\phi_{GMM}$ is the published GMM within-event aleatory variability (without considering directivity), $\phi_{Reduction}$ is the variability reduction model, and $\phi_{i|UH}$ is the added aleatory variability due to the unknown hypocenter (UH) location for a future earthquake. Depending on the application, $\phi_{i|UH}^2$ may be added explicitly or implicitly; see Sections 5 and 6. The total standard deviation to use with the GMM is a combination of Equations 5 and 6.

The model for $\phi_{Reduction}$ is given by Equation 7. The coefficient $e_1(\mathrm{T})$ is listed in Table 4-3 for the simulation-based model (Model 1) and the NGA-W2 data-based model (Model 2). The standard deviation adjustment models are appropriate over the period range 0.01 to 10 seconds, in the magnitude range **M**6.0-8.0, and only apply for sites within the footprint of the directivity model (e.g. for rupture distances less than $R_{max}$; this is built into Equation 7).

$$\phi_{Reduction}(\mathrm{T}, R_{rup}, \boldsymbol{M}) = \begin{cases} e_1(\mathrm{T}) & For\ R_{rup} < R_{max}(\boldsymbol{M}) \\ 0 & For\ R_{rup} \geq R_{max}(\boldsymbol{M}) \end{cases} \tag{7}$$

Table 4-3. Period dependence of $e_1$ for Model 1 and Model 2.

| T (sec) | 0.01 | 0.3 | 0.4 | 0.5 | 0.75 | 1 | 1.5 | 2 | 3 | 4 | 5 | 7.5 | 10 |
|---|---|---|---|---|---|---|---|---|---|---|---|---|---|
| **Model 1 (Simulations) $e_1$** | 0.000 | 0.000 | 0.0003 | 0.011 | 0.038 | 0.072 | 0.107 | 0.143 | 0.172 | 0.189 | 0.195 | 0.206 | 0.200 |
| **Model 2 (NGA-W2) $e_1$** | 0.000 | 0.000 | 0.002 | 0.007 | 0.024 | 0.041 | 0.064 | 0.076 | 0.091 | 0.110 | 0.124 | 0.145 | 0.157 |

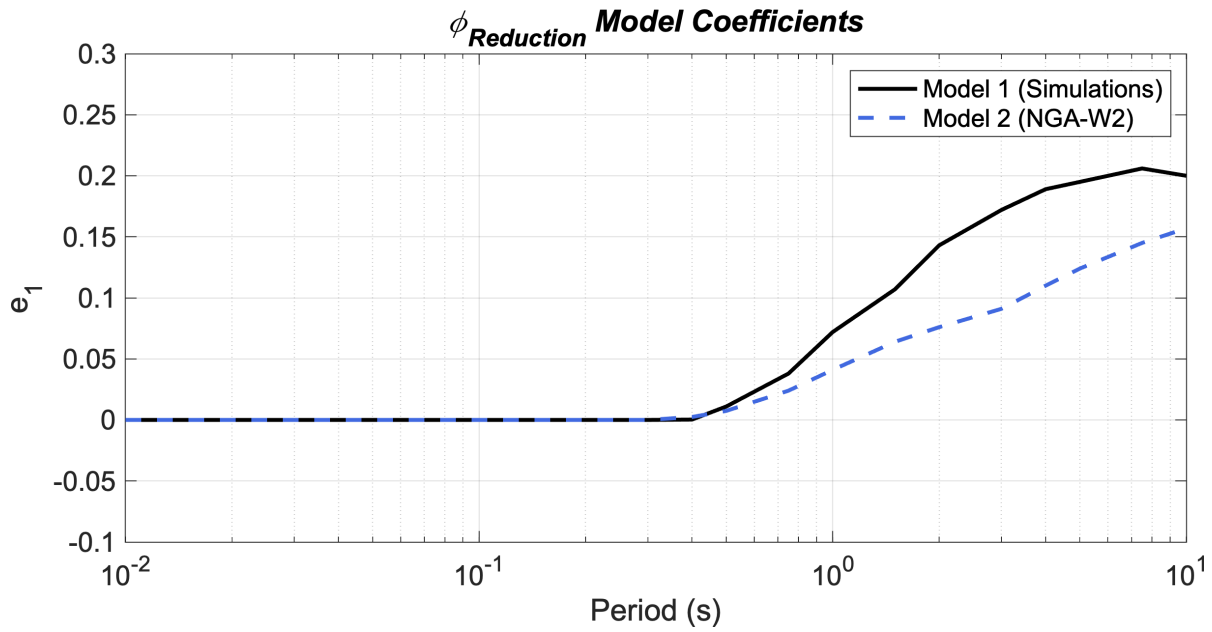


Figure 4-2. Within-event aleatory variability model coefficients versus spectral period.

### *4.4. Model Requirements and Ranges of Applicability*

To use the model requires:

1. Definition of the strike-slip earthquake rupture, which includes **M,** segment coordinates, segment lengths, segment strike angles, the depth to the top of rupture, the rupture representative down-dip width, the rupture representative rake angle, and a primary hypocenter location.
2. The position of the site relative to the rupture, $U$ and $T$, derived from the earthquake description and the site coordinates.
3. The spectral period of interest, T.

Examples of these requirements for a set of earthquake scenarios are given in Appendix E. Appendix A includes MATLAB and FORTRAN scripts/functions for these calculations.

Restrictions are imposed on the geometry of earthquake ruptures, as in Spudich et al. (2013). All fault *segments* are assumed to be rectangular planes with horizontal tops and bottoms, and with a discrete strike angle and dip angle. One or more fault segments compose contiguous fault *strands* (which may model changes in strike and dip), and one or more fault segments compose a complete *rupture*. Multi-fault ruptures are defined and described in Section 6.2. We follow the Aki and Richards (1980) convention where segments always dip to the right when looking along the strike direction, strike angles are measured clockwise from north, and dip angles are less than or equal to 90 degrees.

This formulation, along with use of the GC2 coordinate system, allows application of the model to discontinuous multi-segment ruptures. In this process, the coordinate $U$ is converted to the directivity parameter $S$, and the simple algorithm for $S$ includes the distance between any disconnected ruptures. Therefore, ruptures with relatively large gaps along-strike will experience artificially increased $S$ values in some locations.

The model is designed for strike-slip earthquakes only. In forward application, an earthquake can be categorized as strike-slip if it has representative rake angle falling between one of these ranges: -180 to -150 degrees, -30 to 30 degrees, or 150 to 180 degrees.

The model is appropriate over the period range 0.01 to 10 seconds, for distances up to 80 km from the rupture surface trace (for larger distances there is zero effect). The model is developed using strike-slip earthquakes in the range **M**6.0-7.9. We have tested the model for scenario earthquakes ranging from **M**6.0 to **M**8.0 (Section 6) and are satisfied with the model behavior; therefore we consider it applicable over the range **M**6.0-8.0. Table 3-4 lists a few special constraints imposed on the directivity model parameters. The limits for spectral period, magnitude, and the parameters in Table 3-4 are built into the MATLAB and FORTRAN functions provided in Appendix A.

Table 4-3. Imposed constraints on select parameters.

| Parameter | Constraint | Comment |
|---|---|---|
| $\boldsymbol{S_2}$ | $S_2 \leq 465$ km | Capped at 465 km, assumed to approximately represent the rupture length of a strike-slip $\boldsymbol{M}8$. |
| $\boldsymbol{M}$ | $6.0 \leq \boldsymbol{M} \leq 8.0$ | The model was developed using the range $6.0 \leq \boldsymbol{M} \leq 7.9$, see discussion below. |

The model is developed using residuals calculated from the average of three NGA-West2 GMMs: Abrahamson et al. (2014), Boore et al. (2014), and Campbell and Bozorgnia (2014). Chiou and Youngs (2014) was not included because it contains directivity adjustments. In general, we did not observe large differences between the model developed from residuals using the average of these GMMs versus the models developed from individual GMM residuals. Therefore, in forward application, it is designed to be used with these models on average or individually.

### *4.5. Assumptions and Limitations*

Two limitations from the Bea20 model still remain. First, the simple distance and source depth tapers applied to the directivity effect are not well constrained. These tapers are ad-hoc and are imposed primarily to ensure the model is applied only within the distance ranges that are relevant in seismic hazard and for which the model was calibrated. Spudich and Chiou (2013) note that the distance taper should be a function of period because directivity can be observed at long periods at teleseismic distances, but this behavior is not modeled. Others have also observed rupture directivity effects at large distances in CyberShake simulations (Meng et al., 2023; Bayless and Abrahamson, 2022). Second, the directivity predictors used by the model are ad-hoc and intuitive in nature, and although they appear to work well, this also means that for scenarios (e.g. magnitudes, distances, periods, source-site azimuths, etc) with little data, the model is strongly based on the assumptions about the behavior of these predictors.

The model does not account for differences between the rupture direction and the slip direction. The coefficients include the average effect of differences between the slip direction and the rupture direction. The remaining aleatory term also accounts for this simplification in the model. In reality, the direction of rupture propagation and its consistency with the slip direction will affect the degree of rupture directivity (Aagaard et al., 2004).

Directivity effects are reasonably well studied for strike-slip faults, and they are not well characterized for dip-slip faults (Al Atik et al., 2023; Donahue et al., 2019; Spudich et al., 2013). Donahue et al. (2019) evaluated the similarities and differences among the five Spudich et al., (2013) directivity models for a range of rupture scenarios and found broad consistency in the directivity adjustments to the median ground-motion prediction among the five directivity models for strike-slip scenarios. For reverse scenarios, Donahue et al. (2019) found substantial differences among the five directivity models due to differences in the models' parametrization for these scenarios. These findings are consistent with Spudich et al., (2013).

From these conclusions, it is evident that capturing rupture directivity effects from thrust-faulting earthquakes is difficult. In the current study, we decided not to model directivity for reverse or normal-faulting events because of the following reasons:

- Neutrality issues. The residual analyses are impacted by the neutrality of the directivity condition concepts described in Section 3. The neutrality is a sampling bias issue, and if one imagines a reverse faulting earthquake as a strike-slip earthquake turned on its side, the near-fault recordings stations located on the earth surface are, to some degree, aligned with the rupture plane, and will have a

bias toward positive (up dip) directivity. As a result, directivity effects are captured in the constant term for reverse events (style-of-faulting GMM term).

- Centering issues. Considering a hypothetical pure reverse-faulting earthquake and sites located along the rupture trace (Rx = 0 and Ry0 = 0), the Bea20 model predicts constant amplification for all azimuths. This has the effect of altering the distance scaling of reverse style of faulting earthquakes. If the centering algorithm taken for strike-slip earthquakes is applied to this scenario, $\overline{f_G} = f_G$, and the resulting directivity effect is zero. Therefore, Bea20 will require a reformulation or another centering algorithm for application to reverse and normal style-of-faulting earthquakes.

### *4.6. Changes from Bea20*

This model includes the following significant modifications from Bea20:

- The median directivity adjustment model is centered because its directivity predictor is centered, so there is no change to the median distance or magnitude scaling averaged over all site locations when it is applied to a GMM.
- The usable magnitude range is **M** 6-8.
- There are two alternative versions of the model; one is developed from simulations and the other is from NGA-W2 data.
- The model applies only to strike-slip style-of-faulting earthquakes.

Additionally, the model includes the following implementation changes from Bea20:

- No hypocenter depth dependence.
- Addition of Ztor scaling.
- The distance taper is a function of Rrup instead of the distance from the surface trace (implicitly includes Ztor)
- The origin for the GC2 calculation is the rupture surface trace ordinate of the up-dip projection of the hypocenter.

# 5. Model Implementation: Deterministic

In a deterministic seismic hazard (DSHA) application, the directivity adjustment model can be applied to a GMM without directivity. Deterministic ground-motion percentiles such as the 84th percentile (median plus one standard deviation) should be calculated using $RotD50_{dir}$ and $\phi_{i,Dir}$.

For a given site and earthquake scenario, the simplest application is to specify a hypocenter location, calculate $f_D$, and adjust the GMM median using Equation 1 and the within-event aleatory variability using Equation 6; these equations are repeated in the first row of Table 5-1. Taking this approach, it is possible to estimate the 'worst case' ground-motion scenario by selecting the most onerous hypocenter location, or conversely, the 'best case' scenario by selecting the least demanding hypocenter location. With this method, the parametric variability, $\phi_{i|UH}$, is equal to zero.

Table 5-1. Deterministic implementation of the rupture directivity model for a given earthquake scenario and at a given site.

| Application Method | Median | Within-event Aleatory Variability |
|---|---|---|
| Hypocenter Specified | $\ln(RotD50_{dir}) = \ln(RotD50_{GMM}) + f_D$ | $\phi_{i,Dir}^2 = \phi_{GMM}^2 - \phi_{Reduction}^2$ |
| Hypocenter Unknown (modeled with a distribution) | $\ln(RotD50_{dir}) = \ln(RotD50_{GMM}) + \mu_{f_D}$ | $\phi_{i,Dir}^2 = \phi_{GMM}^2 - \phi_{Reduction}^2 + \phi_{i\|UH}^2$ |

Because the hypocenter locations are not known for future earthquakes, the more appropriate method to use for DSHA is to model the hypocenter locations using a distribution. This is the approach taken in the probabilistic seismic hazard application described in Section 6. When hypocenter locations are modeled in this way, the deterministic ground-motions should be calculated using the equations in the second row of Table 5-1, where the median ground-motion is modified by $\mu_{f_D}$ and the within-event variability has a non-zero parametric variability, $\phi_{i|UH}$.

For a given earthquake scenario and at a given site, $\mu_{f_D}$ is the weighted mean of the median directivity adjustment accounting for the uncertainty in hypocenter location:

$$\mu_{f_D}(\boldsymbol{M},\mathrm{T},x) = \sum_{h=1,N_h} P_h \, f_D(\boldsymbol{M},\mathrm{T},x)_h \tag{8}$$

where $P_h$ is the probability of the $h$'th hypocenter location on the rupture from $N_h$ locations approximating $f_H(h)$ such that $\Sigma_k^{N_h} P_h(h_k) = 1$, and $f_D(\boldsymbol{M},\mathrm{T},x)_h$ is the median directivity adjustment at site location $x$ for hypocenter location $h$.

The parametric variability term $\phi_{i|UH}$ is the added aleatory standard deviation introduced by the distribution of hypocenter locations (because each hypocenter location results in

a different value of $f_D$ at the site). This term, which is a weighted standard deviation, should be calculated directly at each site using Equation 9:

$$\phi_{i|UH}(\boldsymbol{M},\mathrm{T},x) = \sqrt{\frac{\sum_{h=1}^{N_h} P_h\left(f_D(\boldsymbol{M},\mathrm{T},x)_h - \mu_{f_D}(\boldsymbol{M},\mathrm{T},x)\right)^2}{\frac{(N_h' - 1)}{N_h'}\sum_{h=1}^{N_h} P_h}} \quad (9)$$

where $N_h'$ is the number of non-zero weights.

The choice of $f_H(h)$ has epistemic uncertainty and may be modeled as part of the logic tree of the seismic hazard model. Several models for along-strike and down-dip hypocenter distribution are available in the scientific literature (e.g., Mai et al. 2005; Melgar & Hayes, 2019; Watson-Lamprey 2018). Al Atik et al. (2023) used a uniform distribution of hypocenters along strike and down dip.

The following sections provide example applications for the case with a specified hypocenter (5.1), and for the case with an unknown hypocenter (5.2).

## *5.1. Scenario Application with Specified Hypocenter*

The example application of the model here uses the Landers earthquake, modeled with **M** 7.28, total length of 71.7 km, 180-degree rake, 90-degree dip, and $Ztor$ = 0 (Figure 5-1). In this scenario, the hypocenter location is known (or specified). To use the directivity model requires the GC2 strike-normal ($T$) and strike-parallel ($U$) coordinates in km. Figure 5-1 shows maps of the median ground-motions and amplification factors resulting from this scenario for a 3-second spectral period. These maps use the Boore et al. (2014) GMM and assume the reference site and basin conditions in the GMM at all sites.

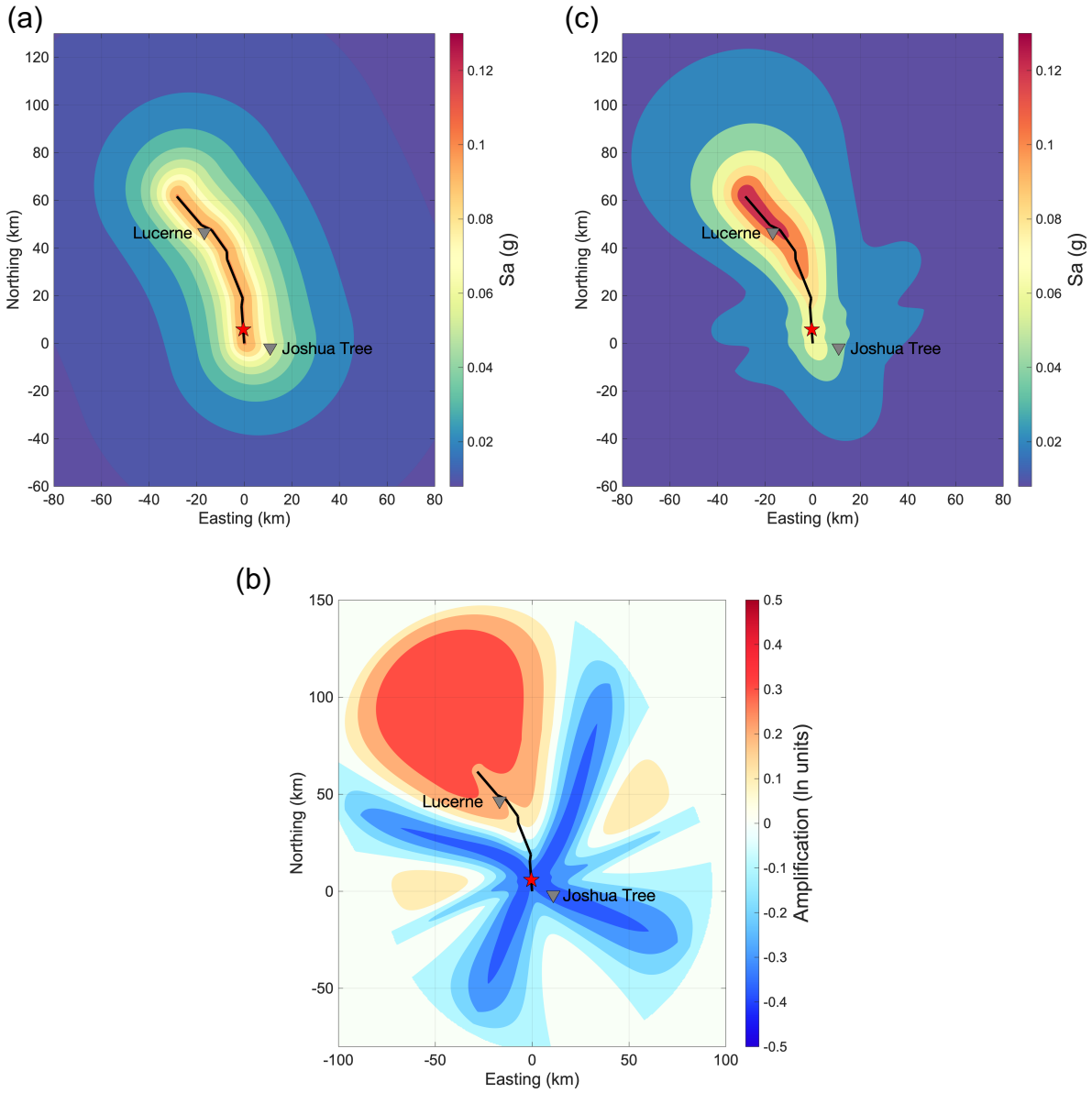


Figure 5-1. Deterministic application of the directivity model, Model 1 median adjustment, to the Landers earthquake with specified hypocenter at 3 seconds spectral period. In all three maps the rupture trace is the heavy black line and the hypocenter location is the red star. (a) Contours of median predicted spectral acceleration from Boore et al. (2014). (b) Contours of $f_D$ for this scenario and spectral period (ln units). (c) Contours of the median predicted spectral acceleration due to adjustment by the $f_D$ values in (b).

Figure 5-1a shows contours of median predicted spectral acceleration from Boore et al. (2014), which do not have azimuthal variation or any correlation with the hypocenter location. Panel b shows contours of $f_D$ for this scenario, hypocenter, and spectral period. Finally, panel c shows the median Boore et al. (2014) spectral acceleration amplified by the $f_D$ values in panel b. Because the hypocenter is near the southern end of the rupture, the region to the north/northwest, including Lucerne, has significantly higher predicted ground-motions after including the directivity adjustment. Conversely, in the backward directivity region (e.g., Joshua Tree), the ground-motions are reduced. Figure 5-2 shows the median response spectra for this scenario at Lucerne and Joshua tree, and Figure 5-3 shows the 84$^{th}$ percentile deterministic response spectra for the scenario using the directivity model median and aleatory variability adjustments (Table 5-1; top row).

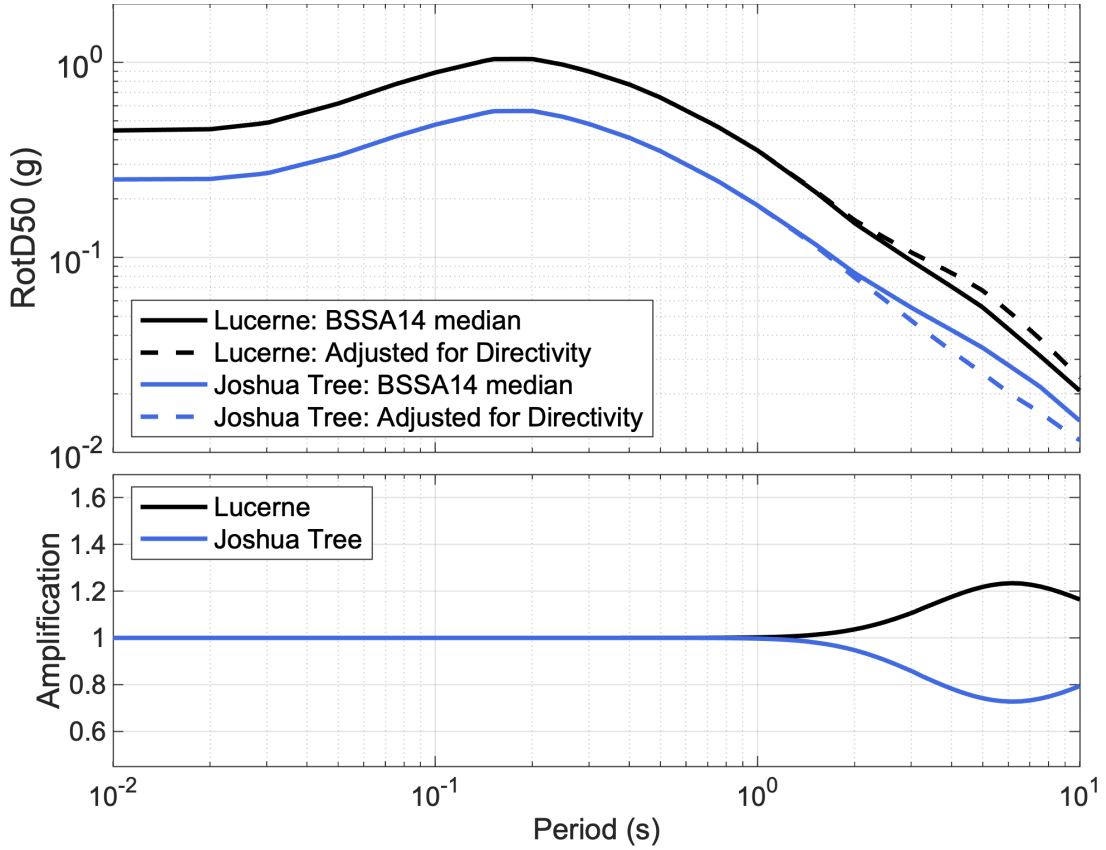


Figure 5-2. Deterministic application of the directivity model, Model 1 for the median adjustment, to the Landers earthquake median response spectra at Lucerne and Joshua tree (locations shown in Figure 5-1).

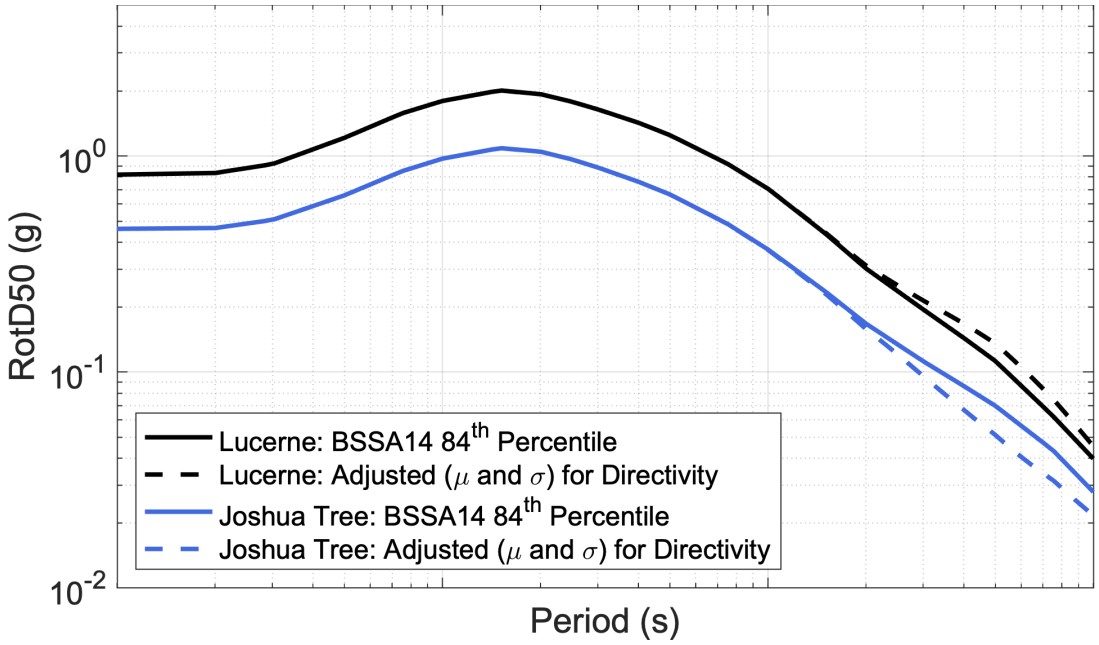


Figure 5-3. Deterministic application of the directivity model, Model 1 for the median and aleatory variability adjustments, to develop the Landers earthquake 84th percentile response spectra at Lucerne and Joshua tree (locations shown in Figure 5-1).

## *5.2. Scenario Application with Unknown Hypocenter*

This section provides a deterministic example with unknown hypocenter location using the same Landers earthquake scenario as in the previous section. We define $N_h = 100$ equally spaced hypocenter locations along-strike and use the Melgar and Hayes (2019) hypocenter distribution model to assign $P_h$ such that such that $\Sigma_k^{N_h} P_h(h_k) = 1$. The directivity model is calculated for each of the 100 hypocenter locations, $h_k$.

Figure 5-4 shows maps of $\mu_{f_D}$ and $\phi_{i|UH}$, which are calculated using Equations 8 and 9, respectively. Using this method, the deterministic ground-motions at a given location are calculated using the equations in the second row of Table 5-1, where the median ground-motion is modified by $\mu_{f_D}$ and the within-event aleatory variability has adjustments $\phi_{Reduction}$ and $\phi_{i|UH}$.

Combining Equations 5 and 6 results in Equation 10:

$$\sigma_{Dir} = \sqrt{\tau_{GMM}^2 + \phi_{GMM}^2 - \phi_{Reduction}^2 + \phi_{i|UH}^2} \qquad (10)$$

Section 3.2 verified that the variability of the directivity effect in the NGA-W2 data reflect a directivity-neutral (unbiased) condition. As a result, $\phi_{i|UH}$ is approximately equal to $\phi_{Reduction}$. The site-specific value of $\phi_{i|UH}$ can be smaller or larger than $\phi_{Reduction}$, but they are approximately equal on average over all azimuths and distances.

In this example, and at T=3 seconds, $\phi_{Reduction} = 0.172$ and $\phi_{i|UH}$ ranges from 0 to about 0.23 in Figure 5-4. Assuming example GMM aleatory standard deviation values of $\tau_{GMM} = 0.35$ and $\phi_{GMM} = 0.6$ ($\sigma_{GMM} = 0.69$), this results in the range of $\sigma_{Dir}$ = 0.67 to 0.71.

At T=7.5 seconds, $\phi_{Reduction} = 0.206$ and $\phi_{i|UH}$ ranges from 0 to about 0.29. Assuming example values of $\tau_{GMM} = 0.3$ and $\phi_{GMM} = 0.6$ ($\sigma_{GMM} = 0.67$), this results in the range of $\sigma_{Dir}$ = 0.64 to 0.70.

Figure 5-5 shows maps of the T=3 sec deterministic ground-motions (median and 84$^{th}$ percentile) with directivity using the unknown hypocenter location method and using the Boore et al. (2014) GMM. These maps have used example GMM aleatory standard deviation values of $\tau_{GMM} = 0.35$ and $\phi_{GMM} = 0.6$ ($\sigma_{GMM} = 0.69$). The spatial pattern of predicted ground-motions in Figure 5-5 are broadly symmetric with respect to the center of the fault trace. This is the result of modeling the future hypocenter locations using a distribution. This symmetry is in contrast with Figure 5-1c, which shows ground-motions for the case of a specified hypocenter location, and results in higher predicted ground-motions to the northwest in the direction on rupture propagation.

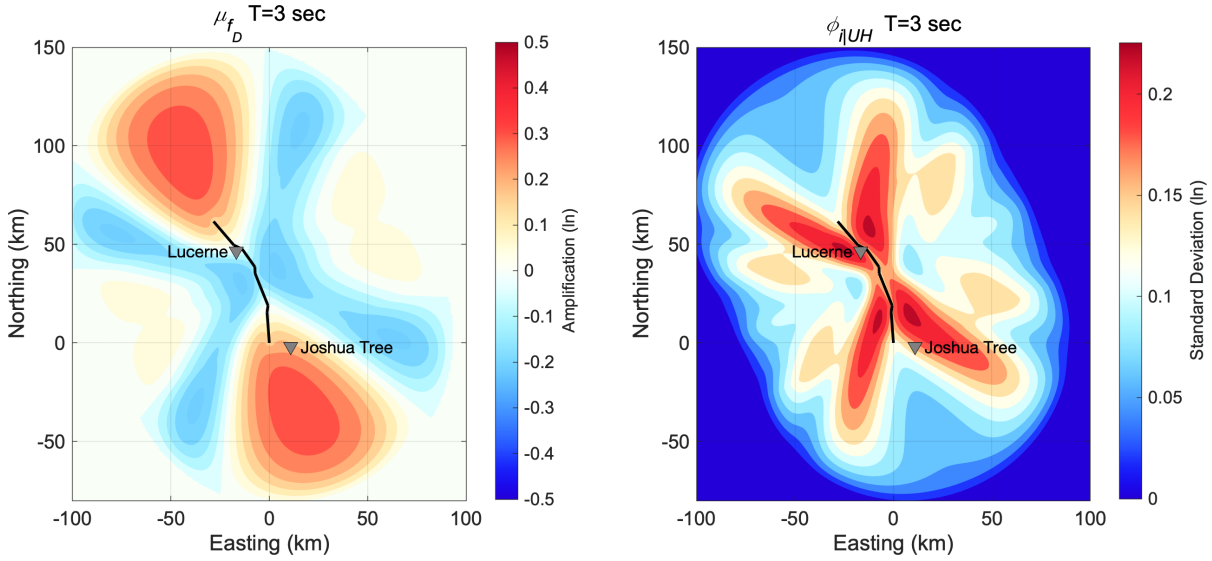


Figure 5-4. Deterministic application of the directivity model (Model 1) to the Landers earthquake scenario with unknown hypocenter location at 3 seconds spectral period. Left: Contours of $\mu_{f_D}$ (ln units). Right: Contours of $\phi_{i|UH}$ (ln units).

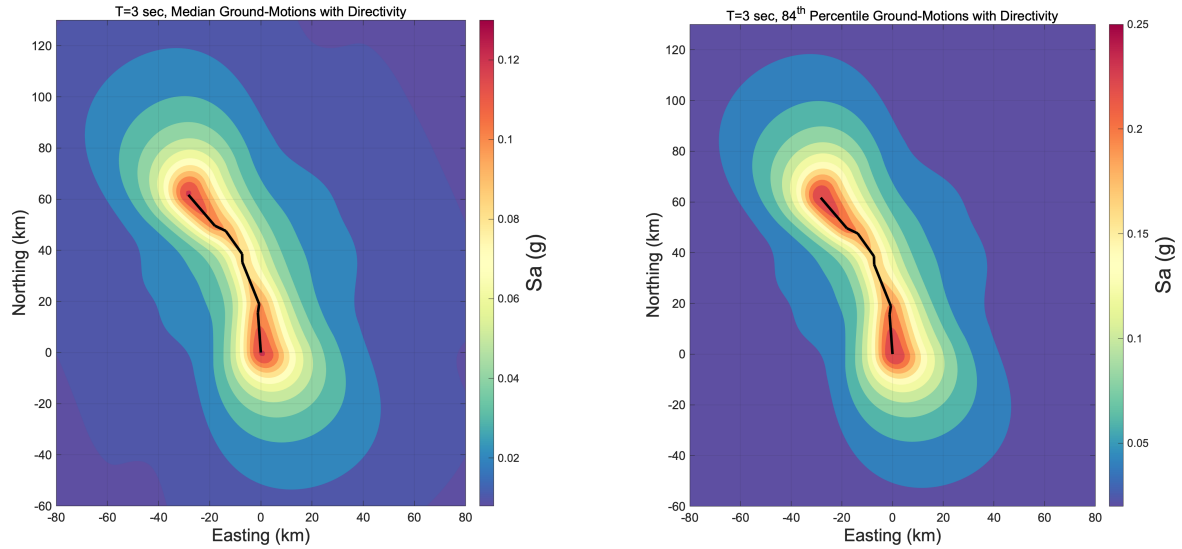


Figure 5-5. Deterministic application of the directivity model (Model 1) to the Landers earthquake scenario with unknown hypocenter location at 3 seconds spectral period, using the Boore et al. (2014) GMM with $\mu_{f_D}$ and $\phi_{i|UH}$ from Figure 5-4, and assuming $\tau_{GMM} = 0.35$ and $\phi_{GMM} = 0.6$. Left: Contours of median predicted spectral acceleration. Right: Contours of the 84th percentile predicted spectral acceleration.

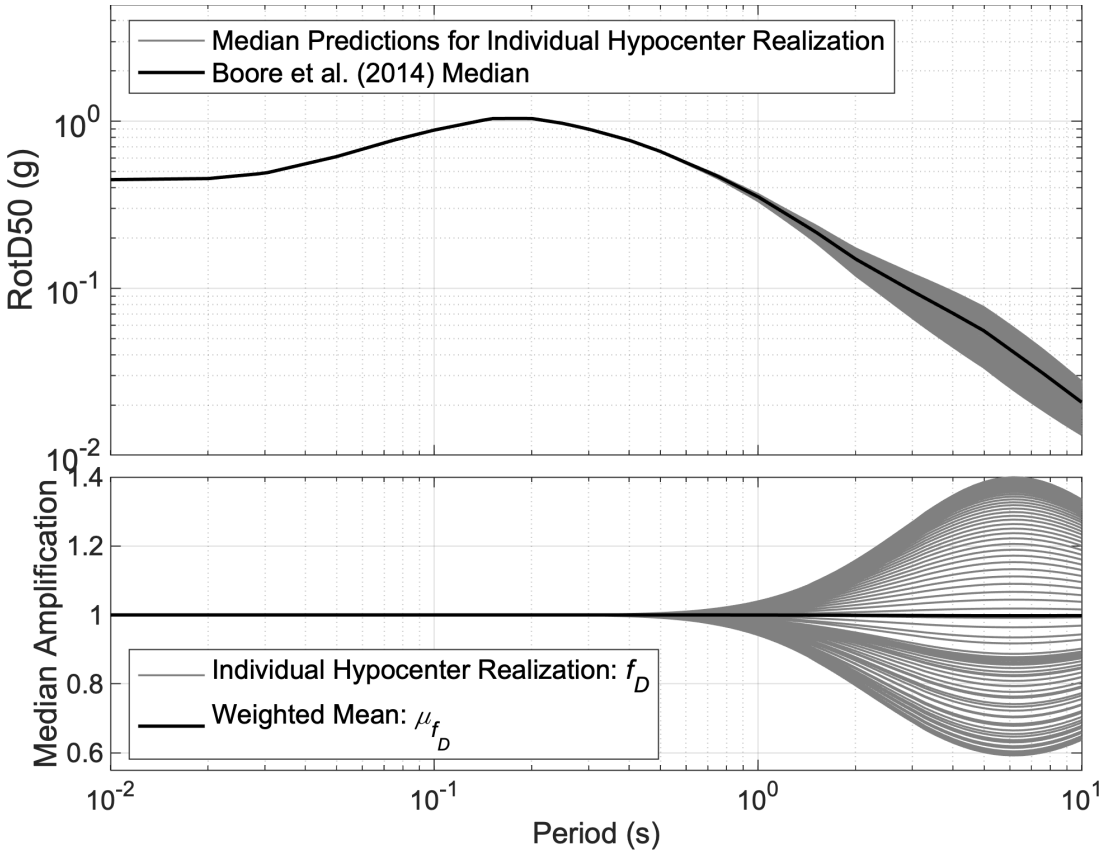


Figure 5-6. Deterministic application of the directivity model (Model 1) to the median ground-motions of the Landers earthquake scenario with unknown hypocenter location at the Lucerne station. Top: Median spectral acceleration from Boore et al. (2014) showing directivity-adjusted spectra for individual hypocenter realizations. Bottom: Median amplification versus spectral period for individual hypocenter realizations (exponential of $f_D$; unweighted) and the weighted mean (exponential of $\mu_{f_D}$).

Figure 5-6 shows median ground-motions at the Lucerne station using the unknown hypocenter location method and the Boore et al. (2014) GMM. The location of this station is shown in Figure 5-4. The top panel of Figure 5-6 shows spectral acceleration from Boore et al. (2014) along with directivity-adjusted median spectra for individual hypocenter realizations. The bottom panel shows the unweighted $\exp(f_D)$ versus spectral period for each of the 100 hypocenter realizations. Because Lucerne is located within the extent of the rupture trace, there are some hypocenters which predict forward-directivity effects (e.g. Figure 5-1), and there are others which predict backward-directivity effects. As a result, $\mu_{f_D}$ is approximately zero (amplification of unity) for this location using the unknown hypocenter location method.

Figure 5-7 compares the components of the total aleatory variability at Lucerne. For this site, $\phi_{i|UH}$ and $\phi_{Reduction}$ are similar; these offset each other and the net aleatory variability adjustment is small (Equation 10). Figure 5-8 shows a contour map of the total aleatory variability adjustment ($\sigma_{Dir} - \sigma_{GMM}$) for this scenario using the unknown hypocenter location approach. This shows how much the 84th percentile changes based on the location due to the change in total aleatory variability.

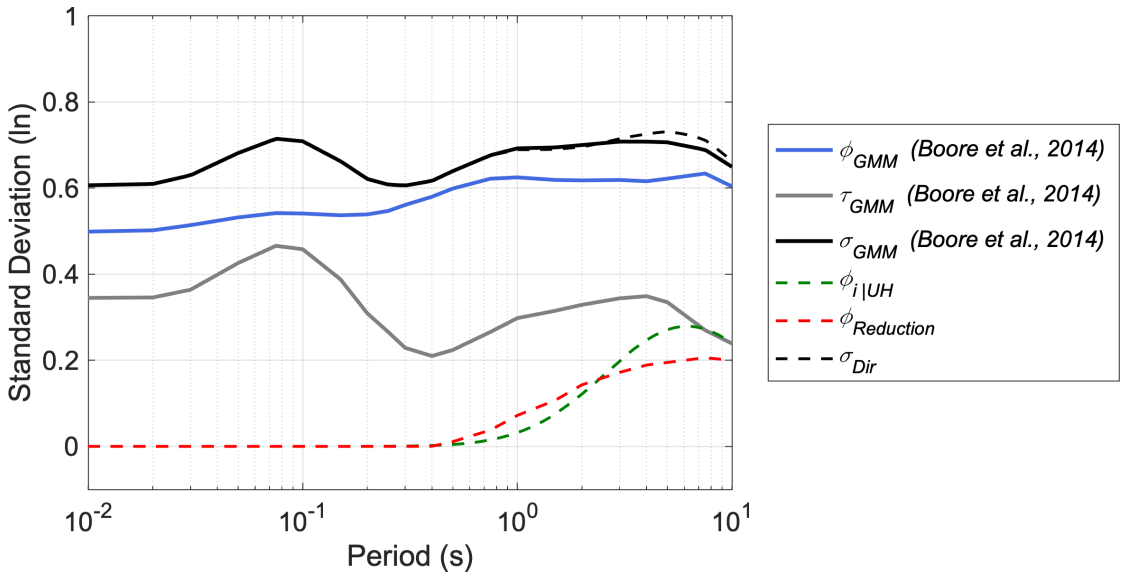


Figure 5-7. Aleatory variability components versus spectral period at the Lucerne station, for the deterministic application of the directivity model (Model 1) to the Landers earthquake scenario with unknown hypocenter location.

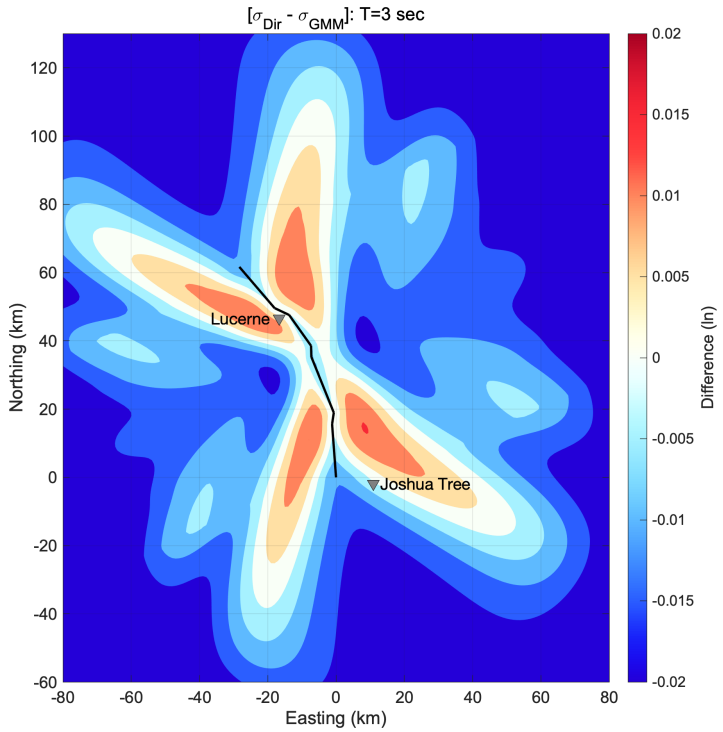


Figure 5-8. Contours of $\sigma_{Dir} - \sigma_{GMM}$ for the deterministic application of the directivity model (Model 1) to the Landers earthquake scenario with unknown hypocenter location.

If the site-specific $\phi_{i|UH}$ is larger than $\phi_{Reduction}$, the net standard deviation adjustment is positive, implying that the variability from directivity for a given site is larger than the range of expected directivity effects from the distribution of stations in the data set (warm colors in Figure 5-8). Alternatively, a net negative adjustment implies the opposite (cool colors in Figure 5-8). Neither has been documented in the literature previously and this has been the main cause of confusion in practice about how to treat directivity effects in PSHA (Donahue et al., 2019). Section 3.2 verified that the variability of the directivity effect in the NGA-W2 data reflect a directivity-neutral (unbiased) condition. As a result, $\phi_{i|UH}$ is approximately equal to $\phi_{Reduction}$. The site-specific value of $\phi_{i|UH}$ can be smaller or larger than $\phi_{Reduction}$, as shown in Figure 5-8, but they are approximately equal on average over all azimuths and distances.

Including directivity effects in a DSHA with unknown hypocenters, there is a small modification to the median and standard deviation as compared to the GMM without directivity. The difference in the deterministic ground-motions can be an increase or decrease compared to the traditional DSHA without explicit consideration of directivity as shown by the maps in Figures 5-5 and 5-8.

# 6. Model Implementation: Probabilistic

## *6.1. Implementation Methods*

In PSHA, the directivity adjustment model can be applied to a GMM without directivity using the same concepts as the deterministic application described in Section 5: for a given earthquake scenario, the GMM is modified using the directivity model median adjustment (Equation 1) and total aleatory variability adjustment (Equation 10). This requires implementation of the directivity model into the PSHA framework, as described here.

The standard PSHA integral for point sources, without considering rupture directivity is (modified from Baker et al., 2021):

$$\lambda(IM > z) = \sum_{i=1}^{n_{src}} N_i(\boldsymbol{M}_{min}) \int_M \int_R P(IM > z|m,r) f_M(m) f_R(r)\ dr\ dm \qquad (11)$$

where $\lambda(IM > z)$ is the annual rate of exceedance of ground-motions with intensity measure (IM) greater than level $z$, $n_{src}$ is the number of earthquake sources considered, $N_i(\boldsymbol{M}_{min})$ is the annual rate of earthquakes with magnitude greater than or equal to $\boldsymbol{M}_{min}$ occurring on source $i$, $P(IM > z|m,r)$ is the conditional probability of observing a IM greater than $z$ for a given earthquake magnitude ($m$) and distance ($r$), and $f_M(m)$ and $f_R(r)$ are probability density functions for the magnitude and distance. $P(IM > z|m,r)$ comes from the GMM and contains an implicit integration over the GMM variability, which is typically modeled by a lognormal distribution.

For planar sources, Equation 11 also needs to consider the finite dimension and location of the rupture within the fault, so four aleatory variables (rupture width, rupture length, along strike location, and down-dip location) and their probability density functions replace the single aleatory variable $r$ and $f_R(r)$ (Abrahamson, 2000). These are omitted here for brevity.

Hypocenter locations are not considered in conventional PSHA (Equation 11) because the traditional GMMs do not utilize the hypocenter location. When rupture directivity effects are modeled, the hypocenter locations need to be introduced. Because the hypocenter locations are not known for future earthquakes, the hypocenter locations need to be modeled using a distribution. If the source characterization includes models for the locations of hypocenters for future earthquakes, Equation 11 can be extended to incorporate rupture directivity effects directly with Equation 12:

$$\lambda(IM > z) = \sum_{i=1}^{n_{src}} N_i(\boldsymbol{M}_{min}) \int_M \int_R \int_H P(IM > z|m,r,\theta_D) f_M(m) f_R(r)\, f_H(\theta_D)\, dr\, dm\, d\theta_D \qquad (12)$$

where $P(IM > x|m,r,\theta_D)$ contains an additional vector of directivity model parameters, $\theta_D$, and there is additional integration over the probability density function for hypocenter location on the rupture plane $f_H(\theta_D)$. $P(IM > z|m,r,\theta_D)$ contains both the median and standard deviation directivity adjustments, and implicit integration over the GMM variability. We refer to this implementation of the rupture directivity model in the PSHA

integral as the *full hypocenter randomization approach*, following the terminology of Donahue et al. (2019) and Weatherill and Lilienkamp (2023).

Sampling the hypocenter locations from a distribution adds substantial computational costs to the hazard calculation because the hypocenters need to be modeled for every relevant fault, and for every relevant rupture (scenario earthquake) hosted on that fault, and directivity parameters need to be calculated for each hypocenter.

Al Atik et al. (2023) applied directivity effects to their PSHA for the state of California using UCERF3 (Field et al., 2013). To implement the full hypocenter randomization approach for each site, they performed a pre-processing step outside of the hazard integral, in which the site-specific directivity parameters were calculated for every UCERF3 rupture and for uniformly distributed hypocenters. The results of this step were saved and used as look-up tables within the main hazard code, which integrates over hypocenter location and accesses the look-up table for each hypocenter. The GMM aleatory variability reduction models for each directivity model were utilized. As a result, at a given site, the mean and variability of the directivity model amplification is captured in the Al Atik et al. (2023) PSHA.

An alternative approach for explicitly modeling directivity in the PSHA integral, as presented by Watson-Lamprey (2018), is called the *modified moments* approach. This approach is to modify the moments of the GMM, for a given rupture based on the probability density function $f_H(\theta_D)$, to reflect the mean changes in the median and aleatory variability due to directivity. This allows for separation of the integration over $f_H(\theta_D)$ from the main PSHA integral and uses the mean and variance of the directivity model amplification to modify the GMM directly (Weatherill and Lilienkamp, 2023). Because of this separation, this approach is appealing for regional scale PSHAs, where the increased computation time required by the full hypocenter randomization approach may be prohibitive (Weatherill and Lilienkamp, 2023). Outside of the hazard integral, the moment modifiers (mean and variance of the directivity model amplification) can be saved using look-up tables or parametric equations.

Several techniques have been employed to determine the moment modifiers outside of the hazard integral: Watson-Lamprey (2018) fit simple parametric equations to directivity amplifications resulting from a synthetic earthquake database, Kelly et al. (2022) fit directivity amplifications from a more robust synthetic earthquake database using machine learning techniques, and Weatherill and Lilienkamp (2023) overfit an artificial neural network to the directivity amplification for each unique rupture in their earthquake rupture forecast. For the latter, the complete set of earthquakes in the forecast must be known a priori. Withers et al. (2024) implemented the Watson-Lamprey (2018) model into the USGS hazard software and tested the impact of including the model on the NSHM results.

The modified moments approach, and related machine learning techniques, are evolving topics and have significant potential for computational efficiencies in regional-scale PSHAs. For site-specific studies, the full hypocenter randomization approach may be more appropriate.

Table 6-1 summarizes the implementation of the directivity model into the PSHA framework for these two approaches. When the full hypocenter randomization approach

is taken, $f_D$ and $\phi_{Reduction}$ are calculated at a site for every hypocenter location of a given rupture; these are part of the term $P(IM > z|m,r,\theta_D)$ from Equation 12. The variability component $\phi_{i|UH}$ is implicit in the integration over $f_H(\theta_D)$. When the modified moments approach is taken, there is no integration over hypocenter location, and $\mu_{f_D}$ and $\phi_{Reduction}$ are calculated at a site for a given rupture. In the modified moments approach, $\phi_{i|UH}$ needs to be added explicitly.

The implementation of Bea24 into HAZ45.2 (Hale et al., 2018; Abrahamson, 2024) is provided in Appendix A. The HAZ45.2 implementation uses the full hypocenter randomization approach.

Table 6-1. Approaches for implementation of the rupture directivity model in PSHA.

| Approach | Median | Within-event Aleatory Variability |
|---|---|---|
| Full hypocenter randomization | $\ln(RotD50_{dir}) = \ln(RotD50_{GMM}) + f_D$<br><br>$f_D$ is calculated for each hypocenter location of a given rupture. | $\phi^2_{i,Dir} = \phi^2_{GMM} - \phi^2_{Reduction}$<br><br>$\phi_{i\|UH}$ is implicit in integration over $f_H(\theta_D)$. |
| Modified moments^ | $\ln(RotD50_{dir}) = \ln(RotD50_{GMM}) + \mu_{f_D}$<br><br>No modeling of hypocenter location; $\mu_{f_D}$ has been determined through integration over $f_H(\theta_D)$ outside the hazard integral. | $\phi^2_{i,Dir} = \phi^2_{GMM} - \phi^2_{Reduction} + \phi^2_{i\|UH}$<br><br>$\phi_{i\|UH}$ is added explicitly. |

^The standard deviation from the modified moments approach has also been called the parametric aleatory term for the GMM (*Abrahamson et al., 1990).*

## *6.2. Treatment of Multi-Fault Ruptures*

The UCERF3 earthquake source model is widely used in the state of California, including for the USGS National Seismic Hazard Maps. UCERF3 includes scenarios that can be categorized as 'multi-fault' ruptures; those with large gaps between segments, significant changes in rupture geometry, changes in the style of faulting along-strike, or a combination of these. In order to apply Bea24 to the UCERF3 and other earthquake forecasts with multi-fault ruptures, a set of rules are required.

Al Atik et al. (2023) was the first attempt to implement current generation directivity models with complex UCERF3 fault ruptures in a statewide framework. Al Atik et al. (2023) defined a multi-fault rupture (having distinct sub-faults) as a rupture that occurs on two or more non-contiguous surfaces with each surface having its own hypocenter, which are distinguished by large changes in dip and rake. A rupture was classified as multi-fault if the change in dip angle between two consecutive subsections exceeds 50 degrees, if the change in the first quadrant rake angle between the same consecutive subsections exceeds 30 degrees, and if the gap between consecutive segments exceeds 10 km.

Ruptures that did not meet the multi-fault rupture criteria were classified as 'multi-segment' ruptures.

Weatherill and Lilienkamp (2023) modified the approach developed by Al Atik et al. (2023) for incorporating multi-fault ruptures into the PSHA. In summary, the ruptures classified as multi-segment are treated in the conventional manner as described in this report (a single hypocenter location distribution on the rupture plane), and the multi-fault ruptures are split up and each sub-fault rupture is characterized individually for rupture directivity effects, including distinct hypocenter location distributions for each. The maximum directivity parameter from each sub-fault is taken to represent the directivity at a given site and for a given multi-fault rupture.

Additional research is needed to evaluate the presence of rupture discontinuities and their impact on rupture directivity as well as the impact of varied multi-fault segment geometries (changes in dip angle, rake angles, and strike direction between sub-faults) on directivity effects (Al Atik et al., 2023). At this time, use of the Weatherill and Lilienkamp (2023) approach for categorizing and modeling multi-fault ruptures is recommended.

### *6.3. Example PSHA*

This section provides an example application of Bea24 in a simple PSHA using the open-source hazard software HAZ45.2 (Hale et al., 2018; Abrahamson, 2024) with the full hypocenter randomization approach. In this PSHA, the Landers earthquake scenario from previous sections is the only source. This source is modeled as a vertical strike-slip fault with 12 mm/yr slip rate and with the maximum-magnitude recurrence model (**M**7.28). The Abrahamson et al. (2014) GMM is used with the reference site and basin conditions. 100 hypocenters spaced evenly along strike are used with a uniform distribution. Bea24 does not have hypocenter depth dependence, so the hypocenters down dip do not need to be modeled. The Bea24 simulation-based model (Model 1) is used including the median and aleatory variability adjustments as in Table 6-1.

The PSHA is performed for two sites: Joshua Tree ($R_{rup}$ = 11.0 km) and Lucerne ($R_{rup}$ = 2.2 km). The sites are located as shown in Figure 5-4.

Figure 6-1 shows the mean hazard curves for T=3 sec at the Joshua Tree and Lucerne sites. The dashed hazard curves have implemented the Bea24 directivity model and solid lines have no treatment of directivity. In this example, the mean hazard without directivity at Lucerne is higher than at Joshua Tree only due to their respective distances from the fault.

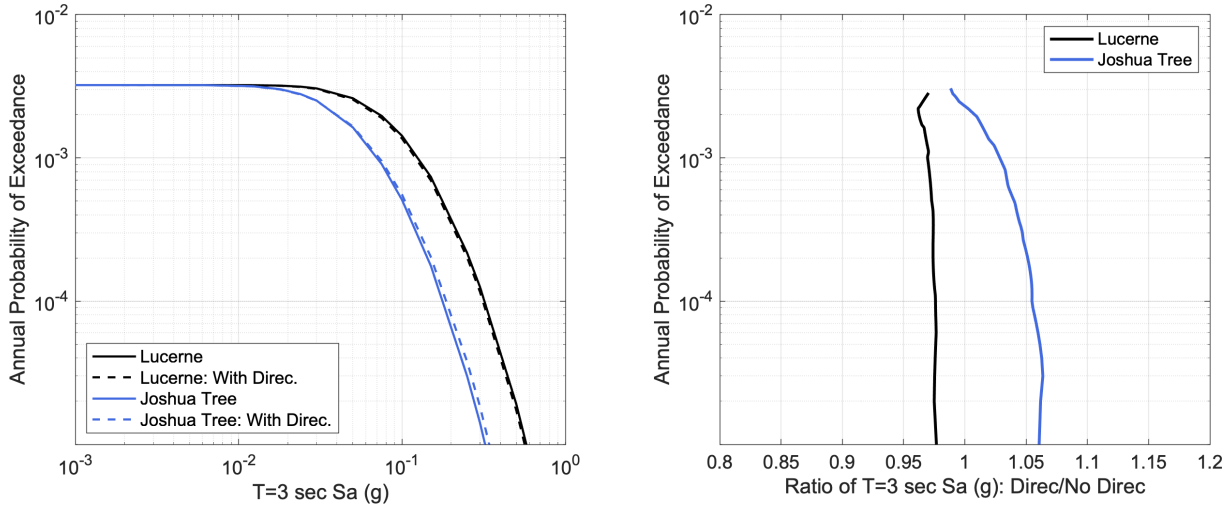


Figure 6-1. Left: T=3 sec mean hazard curves at Lucerne and Joshua Tree stations from the example PSHA, with and without rupture directivity. Right: Ratios of the T=3 sec ground-motions with and without directivity.

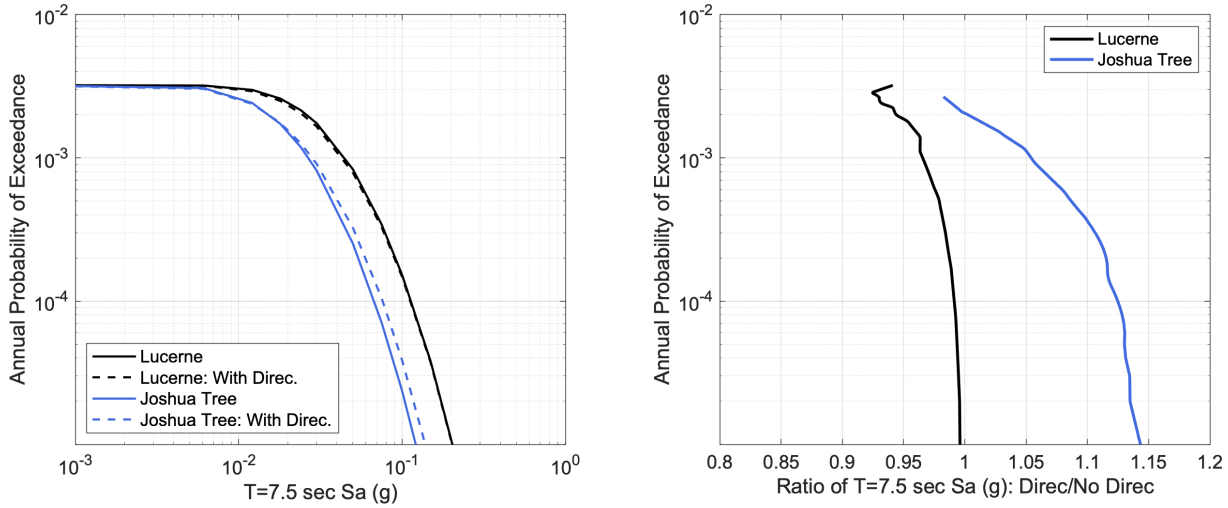


Figure 6-2. As in Figure 6-1, for T=7.5 sec.

The right panel of Figure 6-1 shows ratios of the hazard curve ground-motions versus probability of exceedance, where the ratio is the hazard curve with directivity divided by the hazard curve without directivity. At the Lucerne station, which is located within the extent of the rupture trace, the inclusion of directivity reduces the T=3 sec PSHA ground-motions by a few percent. This is analogous to the deterministic application described in Section 5.2; at this site, there are some hypocenters which predict strong forward-directivity effects, and there are others which predict backward-directivity effects. As a result, the mean adjustment to the median considering the full distribution of future hypocenter locations is a very small reduction. The total change in aleatory variability at this site is also small; less than 0.01 ln unit for T=3 sec (Figure 5-8).

At the Joshua Tree station, which is located off the end of the rupture trace and to the southeast, the inclusion of directivity increases the T=3 sec PSHA ground-motions by up to 6 percent. This is again analogous to the deterministic application described in Section

5.2; at this site, there are a range of median directivity adjustments from the range of potential hypocenter locations, and the mean of these increases the median ground-motions. The total aleatory variability at this site is reduced by less than 0.01 ln units for T=3 sec (Figure 5-8).

Figure 6-2 provides the same comparison for the T=7.5 sec PSHA results, where the impact of including directivity is stronger for the Joshua Tree site and slightly weaker for the Lucerne site. For a **M**7.28, the Bea24 model predicts peak amplification at T=6.2 sec (Equation 4a) so it is expected that Joshua Tree, which is in a forward-directivity region after accounting for hypocenter location uncertainty, will have a stronger impact of directivity at T=7.5 sec than at T=3 sec.

Mean uniform hazard spectra (UHS) with 5,000-year average return period are shown in Figure 6-3 for both sites. The right panel contains ratios of the UHS; these illustrate the period dependence of the directivity effect on the hazard for each site at this return period.

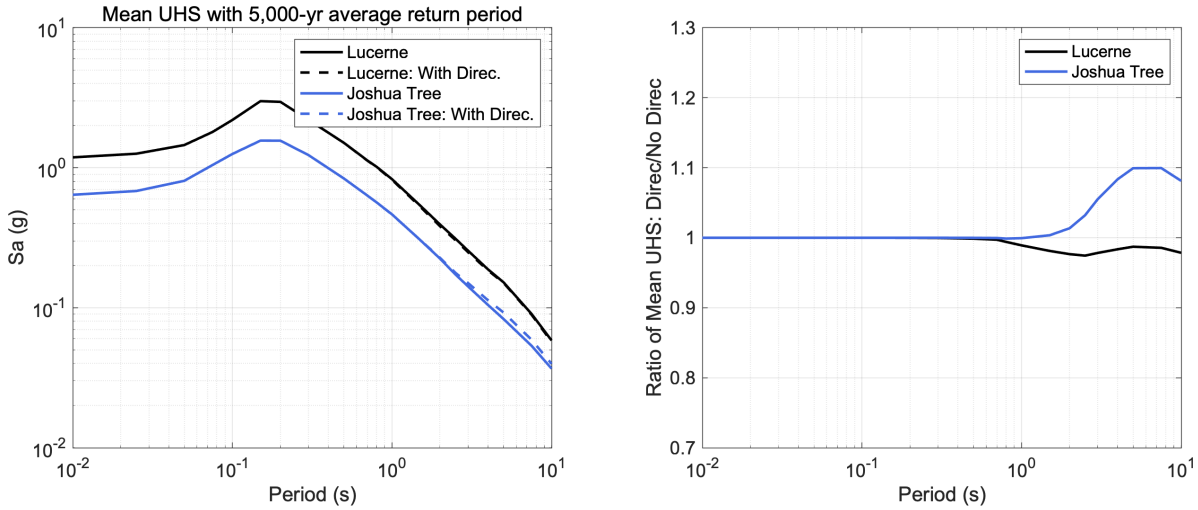


Figure 6-3. Left: Mean UHS with 5,000-year average return period at Lucerne and Joshua Tree stations from the example PSHA, with and without rupture directivity. Right: Ratios of the T=3 sec ground-motions with and without directivity.

Figure 6-4 shows mean T=3 sec hazard curves using the full hypocenter randomization approach but without applying the reduction in aleatory variability ($\phi_{Reduction}$), which is *improper use* of the model and is shown for illustrative purposes only. Without reducing the within-event aleatory variability by $\phi_{Reduction}$, and with the implicit increase in variability from integration over the hypocenter probability density function ($\phi_{i|UH}$), the net result is an increase in total aleatory variability relative to the published GMM variability. This has the effect of artificially decreasing the slope (flattening) the mean hazard curve. To implement the directivity model into the PSHA framework correctly, the GMM aleatory variability should be appropriately reduced as outlined in this report.

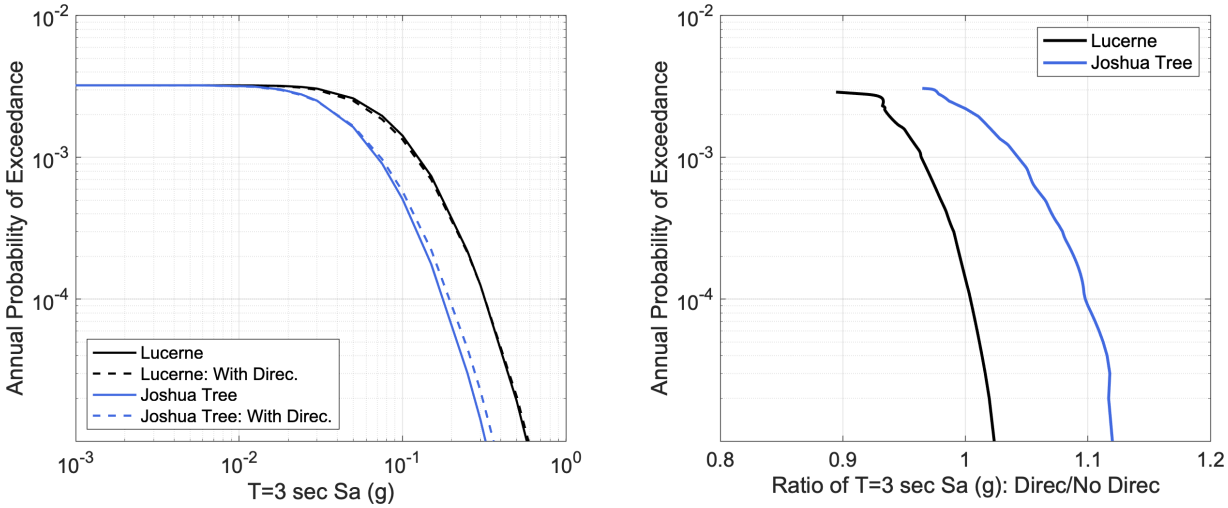


Figure 6-4. As in Figure 6-1, without applying $\phi_{Reduction}$.

# 7. Conclusions

The aim of this study is to provide an updated rupture directivity model and instructions for how to use it in seismic hazard analyses.

As part of these instructions, we clarify the term 'centering' by making a distinction between concepts related to databases (the neutrality of the directivity condition) and to directivity models (centered with respect to the magnitude and distance scaling). We find the mean directivity condition of the NGA-W2 recordings (and GMMs derived from them) have a small bias towards forward directivity. That bias is on the order of approximately 5% at long spectral periods and close distances and is smaller at short spectral periods. The NGA-W2 models can be considered to reflect a directivity-neutral condition of the standard deviation. The Bea24 model is centered for all magnitudes and distances; therefore, applying it to a GMM without directivity does not alter the average magnitude and distance scaling of the GMM.

In this report, we also emphasize that application of the directivity model requires adjustments to both the GMM median and aleatory variability. The variability adjustment has a reduction component, $\phi_{Reduction}$, due to improvements in the median prediction, and an added component, $\phi_{i|UH}$, due to the unknown hypocenter location for a future earthquake. The aleatory variability adjustment depends on the PSHA implementation approach taken. If hypocenter locations are modeled explicitly in the hazard calculation using a probability density function, the effect of the $\phi_{i|UH}$ term is implicitly included. If the mean directivity adjustment has been determined outside the hazard integral, $\phi_{i|UH}$ needs to be added explicitly to the GMM standard deviation. The standard deviation reduction component due to the improved fit, $\phi_{Reduction}$, needs to be incorporated with both approaches.

Implementations of the model in MATLAB (The Mathworks, 2023) and in the open-source hazard software HAZ45.2 (Hale et al., 2018; Abrahamson, 2024) are provided. The HAZ45.2 implementation uses the full hypocenter randomization approach.

There may be an expectation by some that the directivity model should introduce larger changes to the long-period probabilistic hazard than we have shown within this report. The justification behind this perspective is that very large rupture directivity effects have been observed in recorded ground-motions (e.g., the 1987 Loma Prieta, 1992 Landers, California, 1999 Chi-Chi, Taiwan, 1999 Kocaeli, Turkey, 1994 Northridge, California, 1995 Kobe, and 2023 Kahramanmaraş, Turkey earthquakes, especially on the fault-normal component at close distances to the ruptures). These observations are absolutely correct. The reason that changes to the PSHA are smaller than these observations is because the hypocenter locations are not known for future earthquakes, and so we model them using a distribution. For a given site and rupture, there are some hypocenter locations which correspond to ground-motion amplification and there are other hypocenter locations which correspond to de-amplification. The net effect is a smaller change due to directivity than seen for a given hypocenter location.

For a specific scenario (fixed hypocenter), the inclusion of directivity using Bea24 can lead to significant (e.g., $\pm$40-50%) changes in the long-period ground-motion for specific sites, but if the hypocenter locations are randomized for future earthquakes, the net effect

of modeling directivity in the hazard calculation leads to a relatively small change (e.g., ±5-10%) in the ground-motion at return periods of 1,000-10,000 years. The directivity model will be more important for evaluations of past events and for generation of ground-motions for specific scenarios than for PSHA studies.

Capturing rupture directivity effects from thrust-faulting earthquakes is difficult, and the available models for them vary greatly in terms of predicted amplifications; the assumptions of each model in Spudich et al., (2014) had a stronger effect on the predictions than did the data. As a result, this study focuses on strike-slip earthquakes. A future update will address directivity effects for other styles of faulting. A future update may also address directionality by providing models for the fault-normal and fault-parallel orientations (e.g. Somerville et al., 1997).

## 8. Acknowledgements

We thank the Pacific Earthquake Engineering Research Center for making their ground-motion databases, including those from NGA-West2, publicly available. Valuable discussion, feedback, and guidance was received from Linda Al Atik, Nick Gregor, Brian Chiou, Kyle Withers, Brian Kelly, Graeme Weatherill, and Henning Lilienkamp. Finally, we gratefully acknowledge the financial support for this work by the USGS under award number G22AP00199.

## 9. References

Aagaard, B., J.F. Hall, and T.H. Heaton (2004). Effects of Fault Dip and Slip Rake Angles on Near-Source Ground Motions: Why Rupture Directivity was Minimal in the 1999 Chi-Chi, Taiwan Earthquak., Bull. Seismol. Soc. Am., 94: 155-170.

Abrahamson, N.A., P Somerville and C.A. Cornell (1990). Uncertainty in Numerical Strong Motion Predictions. *Proceedings, Fourth U.S. National Conference Earthquake Engineering,* Palm Springs, CA, May 20-24, 1990, Vol. I, pp. 407-416.

Abrahamson, N. A. (2000). Effects of rupture directivity on probabilistic seismic hazard analysis, Proceedings from the 6th International Conference on Seismic Zonation, Palm Springs, California.

Abrahamson N.A., Walter J. Silva, and Ronnie Kamai, (2014). Summary of the ASK14 Ground Motion Relation for Active Crustal Regions. Earthquake Spectra: August 2014, Vol. 30, No. 3, pp. 1025-1055.

Abrahamson, N.A. (2024). HAZ, Github Repository, https://github.com/abrahamson/HAZ

Aki, K. and P. Richards (1980). Quantitative Seismology, Freeman, New York.

Al Atik, L., N. Gregor, S. Mazzoni, and Y. Bozorgnia (2023). Directivity-based probabilistic seismic hazard analysis for the state of California: Report 2, directivity implementation, The B. John Garrick Institute for the Risk Sciences, Technical Report GIRS-2023-05, doi: 10.34948/N3KS3B

Al Atik L, Abrahamson NA, Cotton F, Scherbaum F, Bommer JJ, Kuehn N. (2010). The variability of ground-motion prediction models and its components. Seismological Research Letters; 81(5):794-801.

Ancheta, T.D., Darragh, R.B., Stewart, J.P., Seyhan, E., Silva, W.J., Chiou, B.S.J., Wooddell, K.E., Graves, R.W., Kottke, A.R., Boore, D.M., Kishida, T., Donahue, J.L. (2013). PEER NGA-West2 Database, PEER Report 2013/03.

Baker J, Bradley B, Stafford P. (2021) *Seismic Hazard and Risk Analysis*. Cambridge University Press; https://doi.org/10.1017/9781108425056

Bayless J. and N.A. Abrahamson (2023). Informing Rupture Directivity Modeling with CyberShake Simulations. Final Report. SCEC Award #22056

Bayless, J., and Somerville, P., (2013). Bayless-Somerville Directivity Model, Chapter 3 of PEER Report No. 2013/09, P. Spudich (Editor), Pacific Earthquake Engineering Research Center, Berkeley, CA.

Bayless, J., Somerville, P., Skarlatoudis A. (2020). A Rupture Directivity Adjustment Model Applicable to the NGA-West2 Ground Motion Models and Complex Fault Geometries. Final report. USGS Award No. G18AP00092.

Boore, D. M. (2010). Orientation-independent, non geometric-mean measures of seismic intensity from two horizontal components of motion, Bull. Seismol. Soc. Am. 100, 1830–1835.

Boore, D.M., J.P. Stewart, E. Seyhan, and G.M. Atkinson, (2014). NGA-West2 Equations for Predicting PGA, PGV, and 5% Damped PSA for Shallow Crustal Earthquakes. Earthquake Spectra: August 2014, Vol. 30, No. 3, pp. 1057-1085.

Campbell K.W. and Y. Bozorgnia, (2014). NGA-West2 Ground Motion Model for the Average Horizontal Components of PGA, PGV, and 5% Damped Linear Acceleration Response Spectra. Earthquake Spectra: August 2014, Vol. 30, No. 3, pp. 1087-1115.

Chiou, B. S.-J, and Spudich, P., (2013). The Chiou and Spudich Directivity Predictor DPP, in Chapter 6 of PEER Report No. 2013/09, P. Spudich (Editor), Pacific Earthquake Engineering Research Center, Berkeley, CA.

Chiou, B. S.-J., and Youngs, R. R., (2014). Update of the Chiou and Youngs NGA model for the average horizontal component of peak ground motion and response spectra, Earthquake Spectra 30, 1117–1153.

Donahue, J.L, JP Stewart, N Gregor, Y Bozorgnia (2019) Ground-Motion Directivity Modeling for Seismic Hazard Applications. PEER Report 2019/03

Field, E.H., Biasi, G.P., Bird, P., Dawson, T.E., Felzer, K.R., Jackson, D.D., Johnson, K.M., Jordan, T.H., Madden, C., Michael, A.J., Milner, K.R., Page, M.T., Parsons, T., Powers, P.M., Shaw, B.E., Thatcher, W.R., Weldon, R.J., II, and Zeng, Y., (2013). Uniform California earthquake rupture forecast, version 3 (UCERF3)—The time-independent model: U.S. Geological Survey Open-File Report 2013–1165, 97 p., California Geological Survey Special Report 228, and Southern California Earthquake Center Publication 1792, http://pubs.usgs.gov/of/2013/1165/.

Graves, R.W., and Pitarka, A. (2014). Refinements to the Graves and Pitarka (2010) Broadband Ground-Motion Simulation Method. Seis. Res. Letters. Dec 17, 2014, 12:26. doi: 10.1785/0220140101

Hale C., N. Abrahamson, Y. Bozorgnia (2018). Probabilistic Seismic Hazard Analysis Code Verification, PEER Report No. 2018/03, 139pp.

Kelly, B., K. B. Withers, and M. P. Moschetti (2022). Development of a seismic directivity adjustment model to the median and aleatory variability of ground motion models, AGU Fall Meeting Abstracts, 12–16 December 2022, Chicago, Illinois, U.S.A., 2022AGUFM.S46A.01K

Liou, I.Y., and Abrahamson, N.A. (2024). Aleatory Variability and Epistemic Uncertainty for Ground-Motion Models in PSHA, Submitted to Bulletin of the Seismological Society of America.

Melgar D, and Hayes G (2019). The Correlation Lengths and Hypocentral Positions of Great Earthquakes. Bulletin of the Seismological Society of America. 109(6):2582-2593

Meng, X., C. Goulet, K. Milner, R. Graves, and S. Callaghan (2023). Comparison of Nonergodic Ground-Motion Components from CyberShake and NGA-West2 Datasets in California, Bull. Seismol. Soc. Am. 113(3): 1152-1175. doi: 10.1785/0120220049

Rodriguez-Marek, A., and Cofer, W. (2009) Incorporation to Forward-Directivity into Seismic Hazard Analysis. Report prepared for Transportation Northwest. Report No. TNW2009-02, Research Agreement No. 430846

Rowshandel, B., (2013). Rowshandel's NGA-West2 directivity model, Chapter 3 of PEER Report No. 2013/09, P. Spudich (Editor), Pacific Earthquake Engineering Research Center, Berkeley, CA.

Rowshandel, B. (2018). Directivity Centering of GMPEs and Directivity Models. Eleventh US National Conference on Earthquake Engineering, June 25-29, 2018, Los Angeles, California.

Somerville, P.G., N. Smith, R. Graves and N. Abrahamson (1997). Modification of empirical strong ground motion attenuation relations for the amplitude and duration effects of rupture directivity. *Seismol. Res. Lett*. 68, 199-222.

Somerville, P.G. (2003). Magnitude scaling of the near fault rupture directivity pulse. Physics of the Earth and Planetary Interiors 137, 201-212.

Spudich, P., and Chiou, B. S.-J., (2013). The Spudich and Chiou NGA-West2 directivity model, Chapter 5 of PEER Report No. 2013/09, P. Spudich (Editor), Pacific Earthquake Engineering Research Center, Berkeley, CA.

Spudich, P., and Chiou, B. S.-J., (2015). Strike-Parallel and Strike-Normal Coordinate System Around Geometrically Complicated Rupture Traces- Use by NGA-West2 and Further Improvements. US Geological Survey Open File Report 2015-1028, 28p.

Spudich, P., Bayless, J. R., Baker, J. W., Chiou, B. S.-J., Rowshandel, B., Shahi, S. K., and Somerville, P. G., (2013). Final Report of the NGA-West2 Directivity Working Group, Pacific Earthquake Engineering Research Center Report PEER-2013/09, Berkeley, CA, 130 pp.

Spudich, P., Rowshandel, B., Shahi, S.K., Baker, J.W. and Chiou, B. S-J. (2014). Comparison of NGA-West2 Directivity Models. Earthquake Spectra Aug 2014, Vol. 30, No. 3 pp. 1199-1221

The MathWorks Inc. (2023). MATLAB version: 9.14.0 (R2023a), Natick, Massachusetts: The MathWorks Inc. https://www.mathworks.com

Watson-Lamprey J.A. (2018). Capturing directivity effects in the mean and aleatory variability of the NGA-West 2 ground motion prediction equations, PEER Report No. 2018/04, Pacific Earthquake Engineering Research Center, University of California, Berkeley, CA.

Weatherill G, H Lilienkamp (2023). Capturing Directivity in Probabilistic Seismic Hazard Analysis for New Zealand: Challenges, Implications, and a Machine Learning Approach for Implementation. Bulletin of the Seismological Society of America; doi: https://doi.org/10.1785/0120230161

Withers, K., M. Moschetti, P. Powers, M. Petersen, R. Graves, B.T. Aagaard, A. Baltay, A. Frankel, N. Luco, E. Wirth, S. Rezaeian, E. Thompson. (2024). Evaluation and Integration of Seismic Directivity Models for the USGS National Seismic Hazard Model. Earthquake Spectra

## 10. Bibliography

No publications have resulted from this research as of this date.

## 11. Project Data

This research uses publicly available data from the Pacific Earthquake Engineering Research Center (https://peer.berkeley.edu).

## Appendix A: MATLAB and HAZ45 Model Implementations

The repository https://github.com/jay14bay/USGS_G22AP00199 contains the following MATLAB files:

- Bea24_Example.m: a script which calculates the directivity effect (median and standard deviation) for an example scenario and produces a map, making use of the functions below.
- GC2.m: Calculates the GC2 coordinates. This function is a conversion to MATLAB of Brian Chiou's R functions (pers. comm.)
- Bea24.m: a function which implements the Bea24 directivity model.

The repository https://github.com/jay14bay/USGS_G22AP00199 contains the following files for implementation of the model into HAZ45.2:

- Directivity_bea24.f: a fortran subroutine which implements the directivity model.
- Modified versions of the following HAZ45.2 programs and subroutines: Directivity.f, Haz_main2.f, gc2.f, cldist.f, and declare1.h
- ChangeLog-7Feb2024.txt: a list of the required changes from HAZ45.2 required to implement the model.

## Appendix B: Calculation of $\overline{f_G}$

Equations 3-3c (repeated below) require the calculation of the directivity predictor centering term at a given rupture distance, $\overline{f_G}$, defined as the mean $f_G$ value over a suite of sites located at the same distance to an earthquake over all azimuths (sites on a racetrack). The value of $\overline{f_G}$ is specific to a scenario with given hypocenter location, rupture dimensions, and rupture distance, Rrup.

$$f'_G = [\, f_G - \overline{f_G} \,]\ f_{dist}\, f_{Ztor}$$

$$f_G = \ln(S_2)\, |\cos(2\theta)|$$

$$S_2 = \sqrt{9 + (S\cos(Rake))^2}$$

$$\theta = \left|\tan^{-1}\frac{T}{U}\right|;\ if\ T = U = 0;\ \theta = 0$$

There are several ways the calculation of $\overline{f_G}$ can be approached for a given racetrack:

1. Closed form (analytic) solution. Solve for the mean value of $f_G$ using the Fundamental Theorem of Calculus (Mean Value Theorem). The mean value is the definite integral of the continuous function $f_G$.
2. Numerical method. Solve for the mean value of $f_G$ numerically.
3. Functional form method. Create a model for $\overline{f_G}$ which approximates.

The closed form solution is preferable to the other methods because it will be exact and efficient to calculate. We attempted to solve the integrals defined below, first by hand, and then with integral solver software available online, but the solutions were extremely complex and seemed unnecessary. We found it was most straightforward to use the numerical method and approximately solve the integrals by splitting the racetrack into four regions, as shown below.

Al Atik et al., (2023) used the functional form method for their statewide hazard analysis with $\Delta DPP$ (Chiou and Youngs, 2014). Al Atik et al., (2023) created a database of scenario earthquakes with a range of rupture dimensions and hypocenter locations and used a functional form to fit a model for $\overline{\Delta DPP}$ given the hypocenter location, rupture distance, and rupture length. This approach is straightforward to apply but may be subject to the largest errors out of the three methods.

Regions 1 and 2: between the fault ends

The figure below shows the map view of a scenario vertical strike-slip rupture (red) with coordinate system origin at the hypocenter (star). The along-strike dimension is x and the strike perpendicular dimension is y. Region 1 is between the origin and the end of the rupture in the along strike direction ($x = L_1$). Region 2 is between the origin and the end of the rupture in the anti-strike direction ($x = -L_2$).

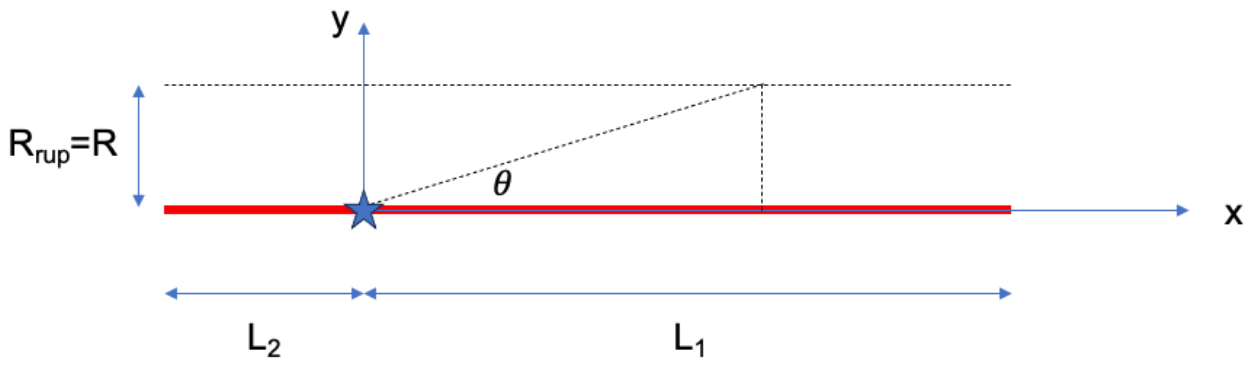


Considering the racetrack at rupture distance R, and setting the rake angle to zero, the following result from Equations 2a-2c for the along-strike direction:

$$\theta(x) = \tan^{-1}(R/x)$$

$$S_2(x) = \sqrt{9 + x^2}$$

$$f_G(x) = \ln(S_2)|\cos(2\theta)|$$

Substituting and integrating $f_G(x)$, we have for Region 1:

$$I_1 = \int_0^{L_1} \ln\left(\sqrt{9 + x^2}\right) |\cos(2\tan^{-1}(R/x))| \, dx$$

For the anti-strike direction (Region 2), equivalently:

$$I_2 = \int_0^{L_2} \ln\left(\sqrt{9 + x^2}\right) |\cos(2\tan^{-1}(R/x))| \, dx$$

Regions 3 and 4: off the fault ends

Off the ends of the fault, $S_2(x)$ is constant and $\theta(x)$ decreases with increasing $x$ because the racetrack curves towards the along-strike direction. Region 3 has $x > L_1$ and Region 4 has $x < -L_2$ (not shown).

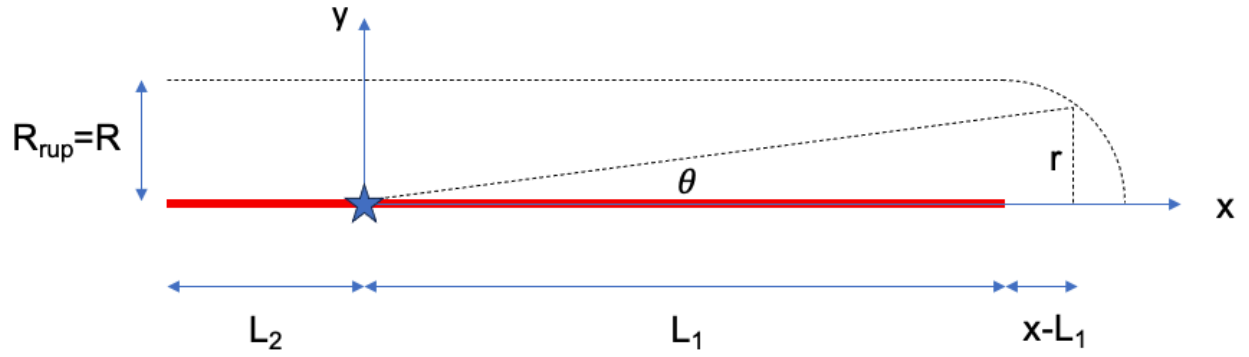


For Region 3, the following result from Equations 2a-2c:

$$r(x) = \sqrt{R^2 - (x - L_1)^2} \text{ (circle formula)}$$

$$\theta(x) = \tan^{-1}(r/x)$$

$$S_2(x) = L_1$$

$$f_G(x) = \ln(S_2)|\cos(2\theta)|$$

Substituting and integrating, we have:

$$I_3 = \ln(\mathrm{L}_1) \int_{L_1}^{L_1+R} \left|\cos\left(2\tan^{-1}\left(\sqrt{R^2-(x-L_1)^2}/x\right)\right)\right| \mathrm{d}x$$

For the anti-strike direction (Region 4), equivalently:

$$I_4 = \ln(\mathrm{L}_2) \int_{L_2}^{L_2+R} \left|\cos\left(2\tan^{-1}\left(\sqrt{R^2-(x-L_2)^2}/x\right)\right)\right| \mathrm{d}x$$

Combination

Using the Mean Value Theorem, $\overline{f_G}$ is the definite integral of the continuous function $f_G$ divided by the interval length, or equivalently:

$$\overline{f_G} = \frac{I_1+I_2+I_3+I_4}{L_1+L_2+R+R}$$

If solved, this would represent the closed form solution. Only one side of the fault is included in this calculation because of symmetry.

In the Matlab implementation of the model provided with this report, the numerical method is used. In this method, the integrands of $I_1$, $I_2$, $I_3$, and $I_4$ are calculated numerically for sites using the spacing $dx$ = 0.1 km, and the mean value for sites in all four regions is computed.

## Appendix C: Median Model Development

The median model is developed following a similar approach taken as in Bea20. The approach utilizes within-event residuals and fits a parametric model relating the Bea24 directivity predictor ($f_G'$) to these residuals to model the directivity effect ($f_D$) and its period-dependence. Residuals are for the RotD50 (Boore et al., 2010) horizontal component of 5% damped spectral acceleration, calculated from three NGA-W2 GMMs (Abrahamson et al., 2014; Boore et al., 2014; Campbell and Bozorgnia, 2014). Two databases are used: one from the suite of simulations described in Bea20, and the second from NGA-W2 recordings of strike-slip earthquakes with a finite fault model and at least 5 recordings.

The steps taken to develop the median model are performed on both databases (simulated and recorded) separately. The steps are:

For each event:

1. Calculate the value Bea24 centered directivity predictor ($f_G'$) at each site where there is data (recorded or simulated).
2. For each spectral period, use the residuals to fit the free parameters from Equation 2: $k$ and $A$. The limiting upper and lower bound of $f_D$ is $\pm A$, and $k$ represents the slope of the relationship between $f_G{}'$ and $f_D$.

Considering all events:

3. Evaluate the magnitude and period dependence of $k$ and of the peak value of $A$ ($A_{max}$).
4. Evaluate and model the magnitude dependence of the period corresponding to $A_{max}$ ($T_{\mathrm{peak}}$; Equation 4a)
5. Model $A$ with a Gaussian function of period (Equation 4). This function has maximum value $A_{max}$ and is centered on period $T_{peak}$. The standard deviation (width parameter) of the Gaussian function is $\sigma_g$.
6. Perform a nonlinear least squares regression using the database residuals to derive the period-independent model coefficients $A_{max}$ and $k$. These coefficients are estimated by a joint regression with combined data of all periods.

The final step (regression) was performed for both datasets independently to inform the rupture directivity modeling. We found that the simulations, which have significantly more near-fault stations and better azimuthal coverage than the data, demonstrate stronger scaling with the directivity parameters and over a broader period range. The NGA-W2 data generally demonstrate weaker scaling over a narrower period range. As a result, directivity model coefficients are provided based on both datasets. The models derived from both datasets have the same functional form and only differ in their coefficients.

Simulations

Figure C-1 provides an example of Step 2 for the Landers earthquake simulation using the Graves and Pitarka (2014) simulation method; the simulations are described in Bea20. This figure shows within-event residuals ($\delta WS_{es}$; blue) versus $f_G'$ at T=6.5 sec. Binned means with 95% confidence interval for small intervals of $f_G'$ are shown in red. The model for $f_D$ fit to the simulation residuals shown (at this period) is given by the dashed green line. The final Bea24 $f_D$ model (Model 1; resulting from Step 7) is shown in black. By applying the final Bea24 model to these residuals, the within-event residual standard deviation reduces from 0.53 to 0.39 natural log units. As described in the above approach outline, Step 2 is repeated for each event and spectral period.

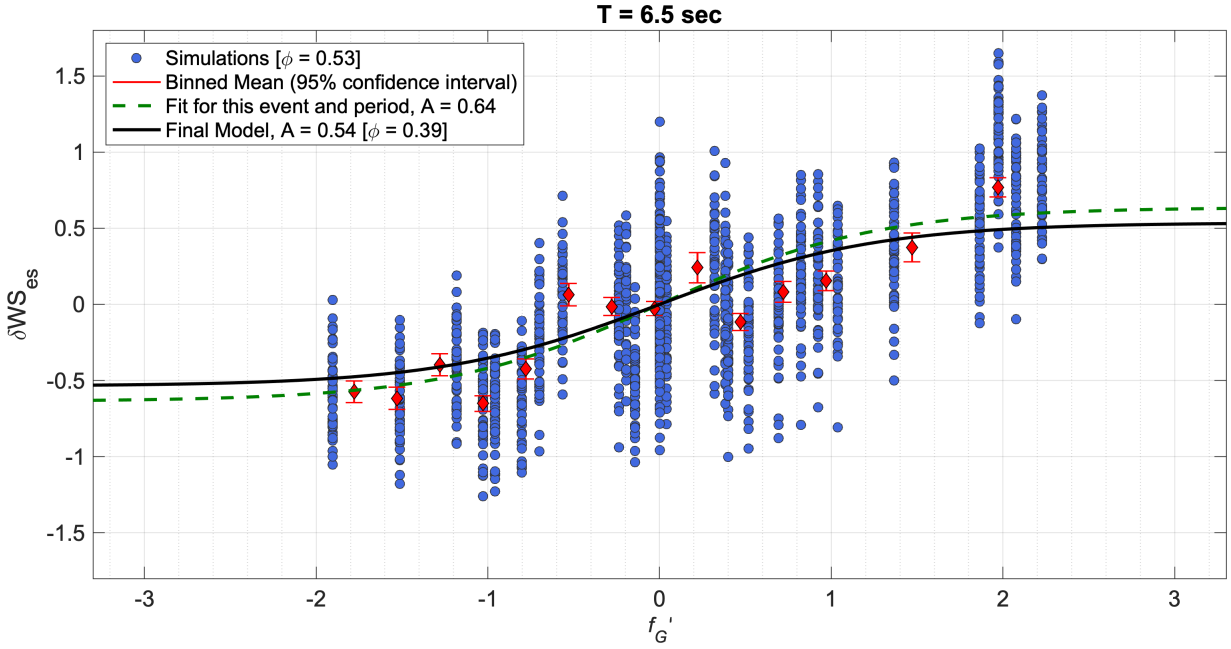


Figure C-1. Summary of Step 2 for the Landers earthquake simulation, at T=6.5 sec.

Figure C-2 summarizes the results of Step 3 for the simulated database, where each line color or marker represents one of the 8 simulated events. Figure C-3 (upper panel) shows Step 4, and the lower panel shows Step 5. The standard deviation (width parameter) of the Gaussian function is $\sigma_g = 0.38$.

Figure C-4 shows within-event residuals ($\delta WS_{es}$) versus $f_G'$ at period $T_{peak}$ (this period varies by event) from complete set of the simulations. Binned means with 95% confidence interval for small intervals of $f_G'$ are shown in red. The Bea24 median model (result of Step 6) is shown in black, with the value of $A_{max}$ determined from the regression. Use of the logistic function saturates $f_D$ for extreme values of $f_G'$; this causes the flattening of the black curve.

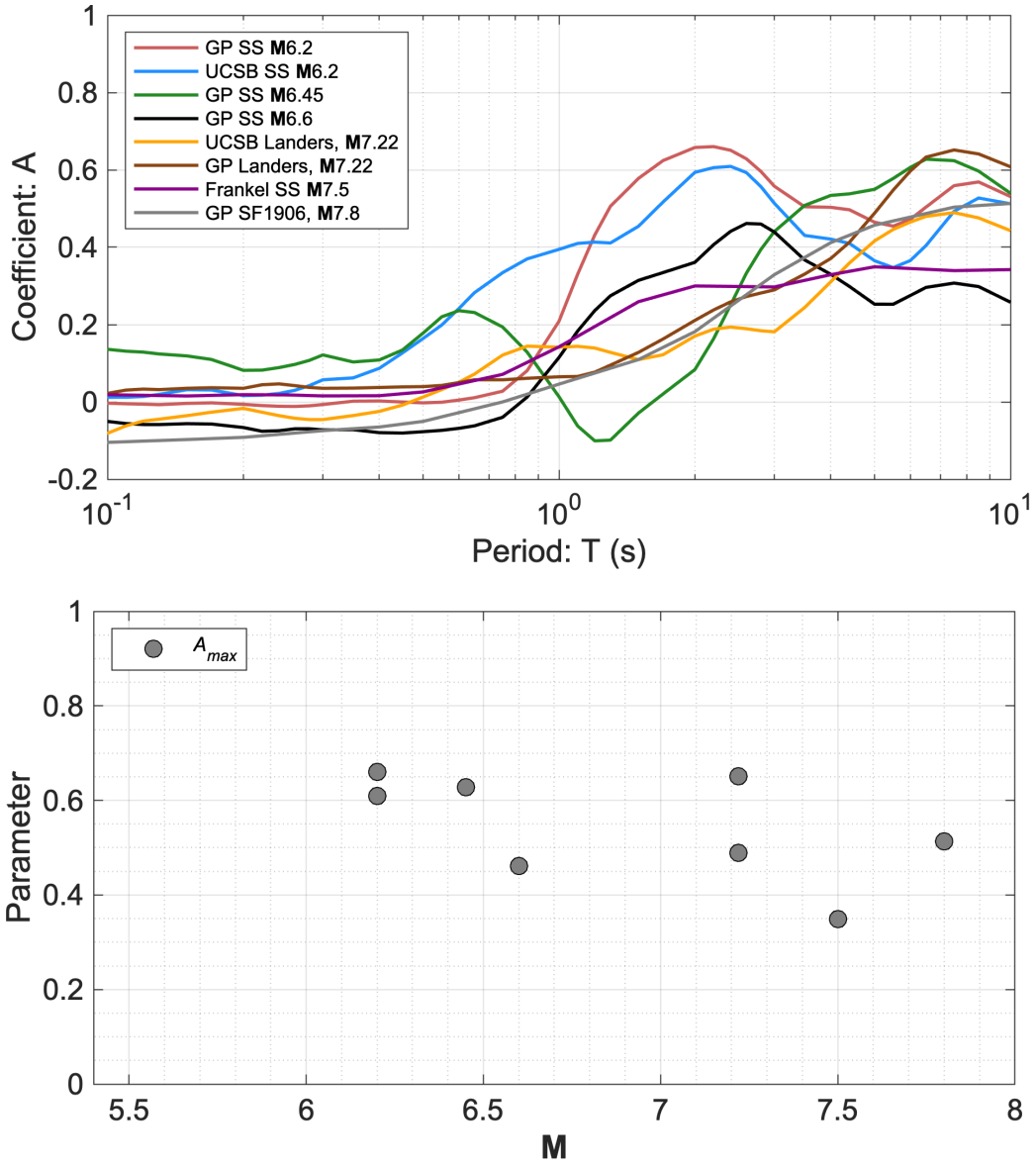


Figure C-2. Summary of Step 3 for the simulated dataset.

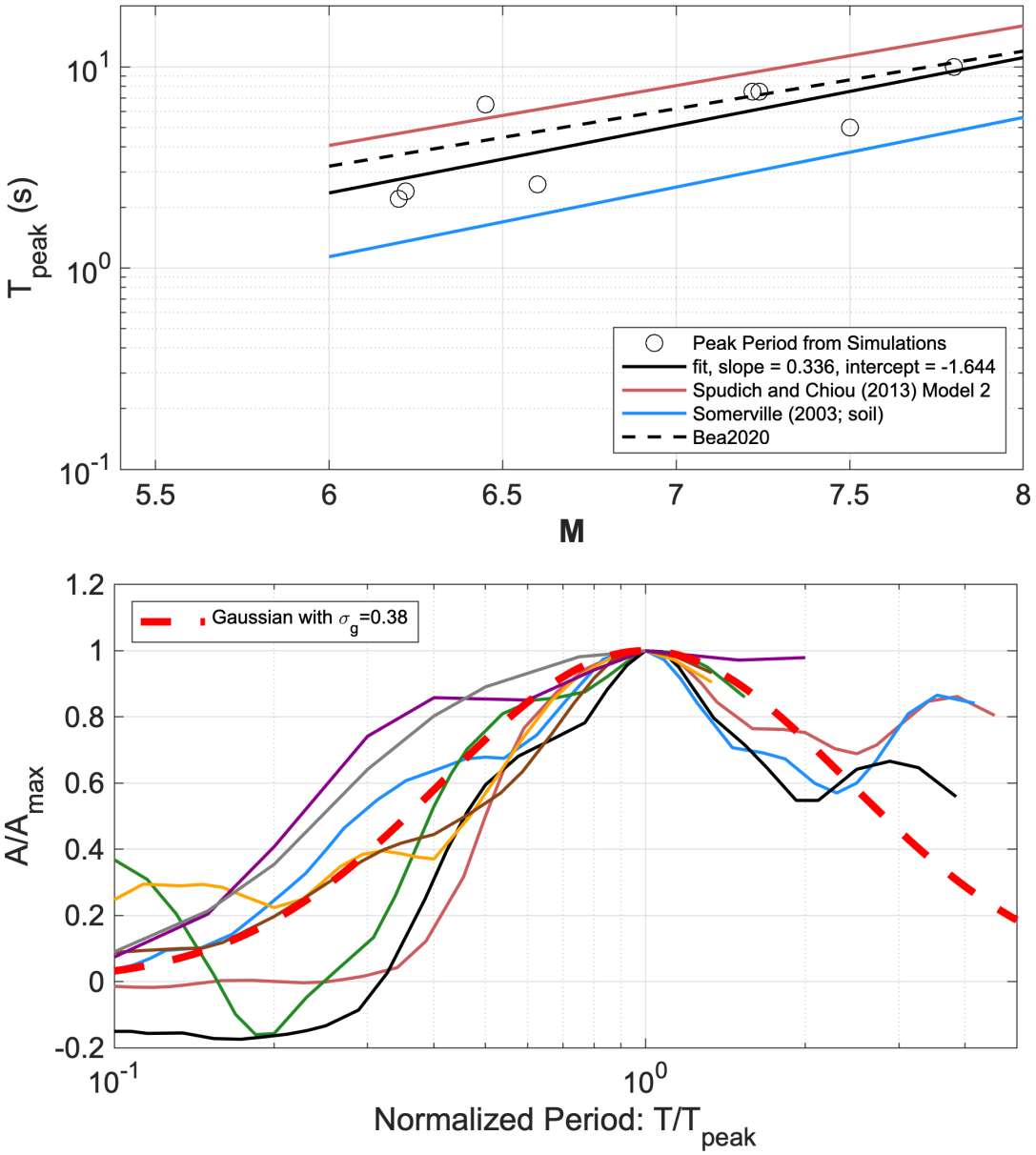


Figure C-3. Summary of Steps 4-5 for the simulated dataset.

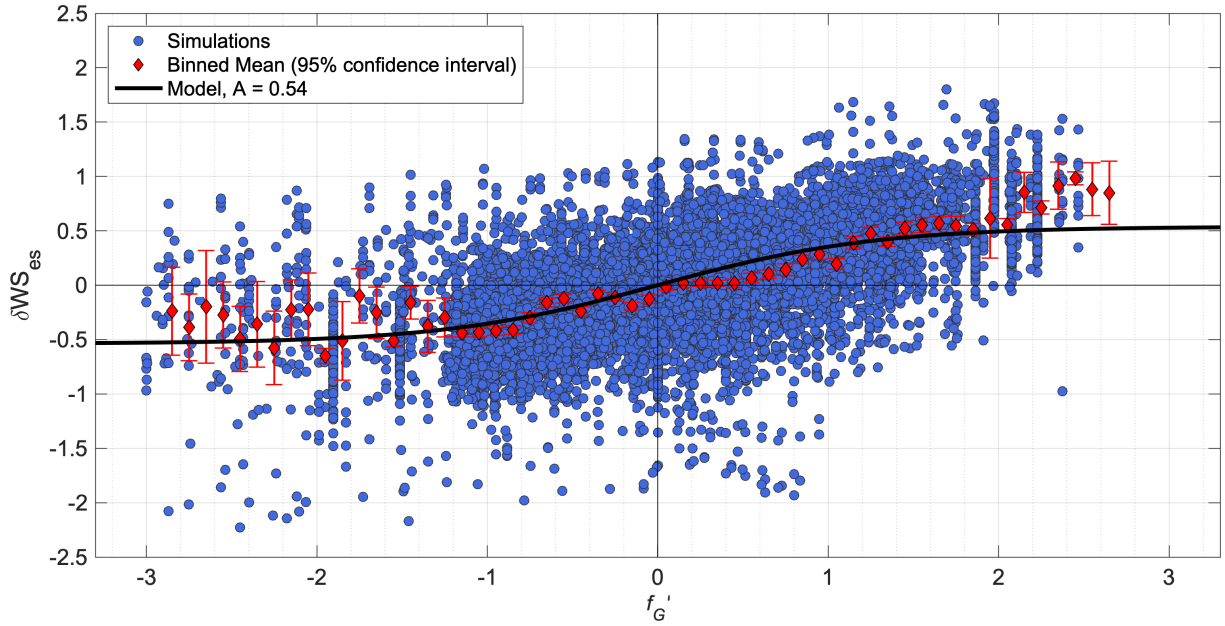


Figure C-4. Within-event residuals ($\delta WS_{es}$) versus $f_G'$ at period $T_{peak}$ (this period varies by event) from the simulations. Binned means with 95% confidence interval for small intervals of $f_G'$ are shown in red. The Bea24 median model from the simulations (Model 1) is shown in black.

NGA-W2

Figure C-5 summarizes Steps 3-5 as applied to the NGA-W2 data. Figure C-6 shows within-event residuals ($\delta WS_{es}$) versus $f_G'$ at period $T_{peak}$ (this period varies by event) from the recorded data. Binned means with 95% confidence interval for small intervals of $f_G'$ are shown in red. The Bea24 median model from the recorded data (Model 2; result of Step 5) is shown in the solid black, and the model from simulations (Model 1) is given by the dashed line.

Simulated and Recorded events

Figure C-7 summarizes the model approach for the combined dataset, where simulations are in grey and recorded events are in blue. Panel a shows the period dependence of $A$ (Step 3), panel b shows the Gaussian function of period used to model $A$ (Step 5), panel c shows the evaluation for magnitude dependence of $A_{max}$ (Step 3), and panel d shows the magnitude dependence of $T_{peak}$ (Step 4).

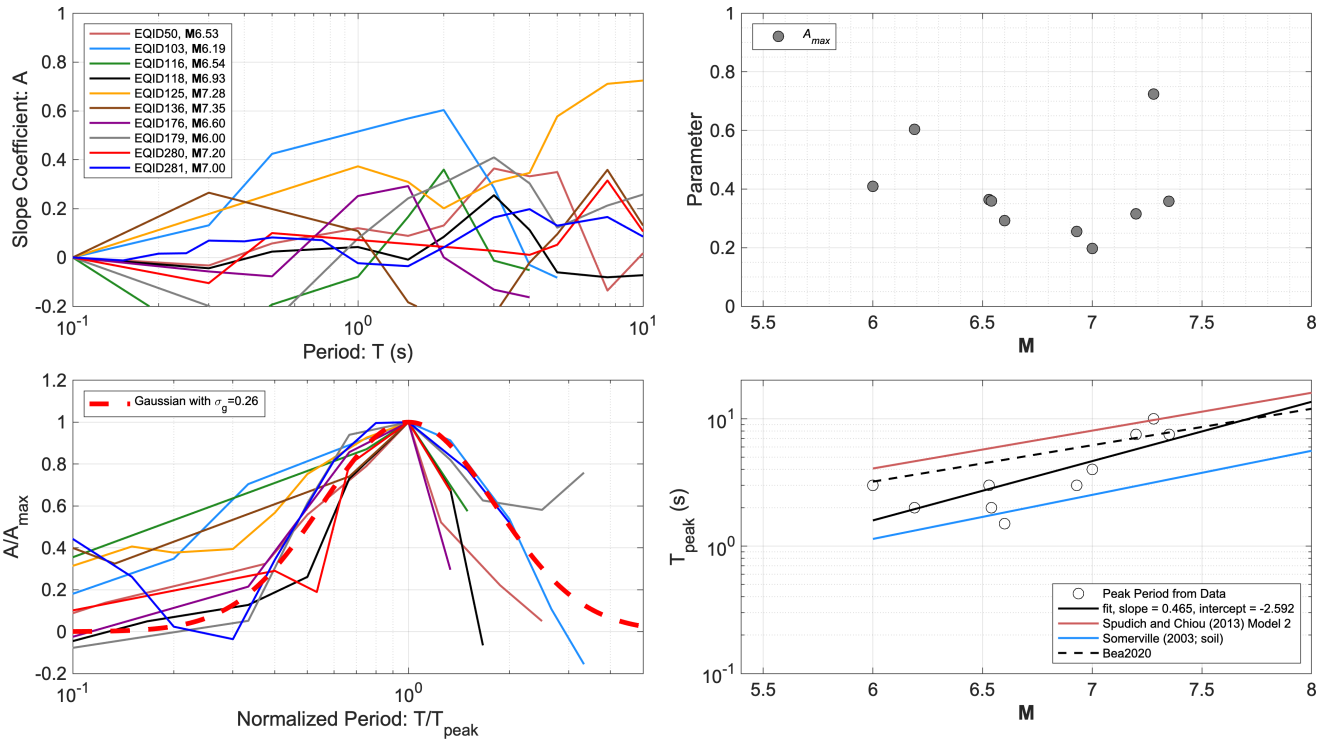


Figure C-5. Summary of Steps 3-5 for the recorded dataset.

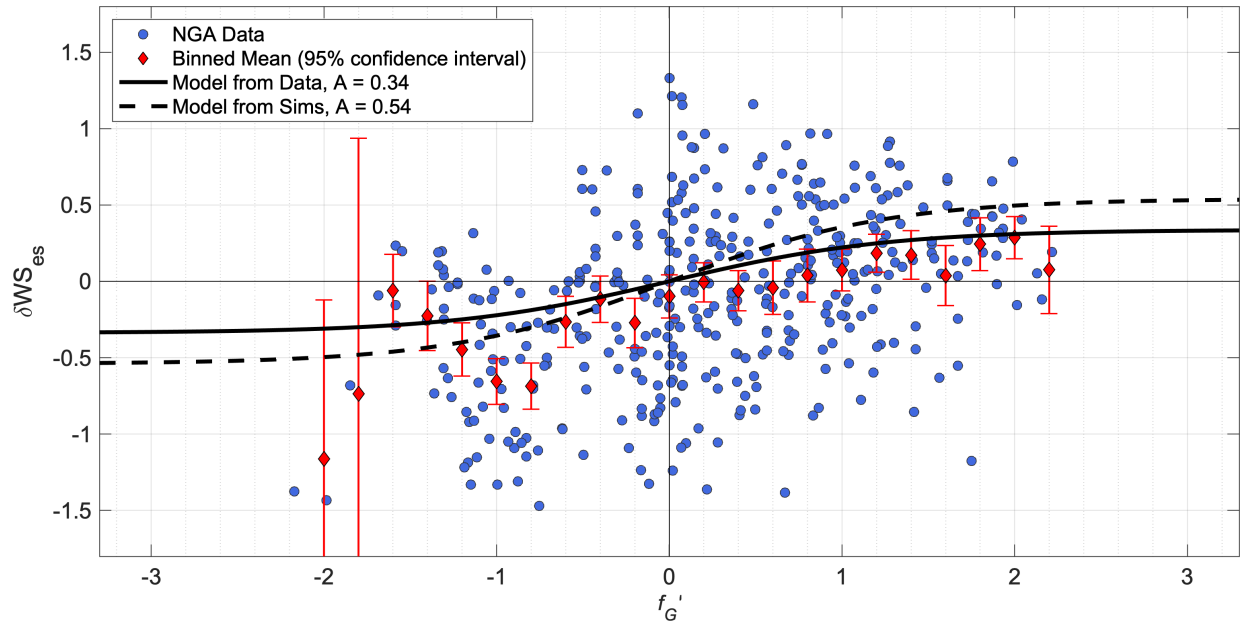


Figure C-6. Within-event residuals ($\delta WS_{es}$) versus $f_G'$ at period $T_{peak}$ (this period varies by event) from the recorded dataset. Binned means with 95% confidence interval for small intervals of $f_G'$ are shown in red. The Bea24 median model from the recorded data (Model 2) is shown in the solid black, and the model from simulations (Model 1) is given by the dashed line.

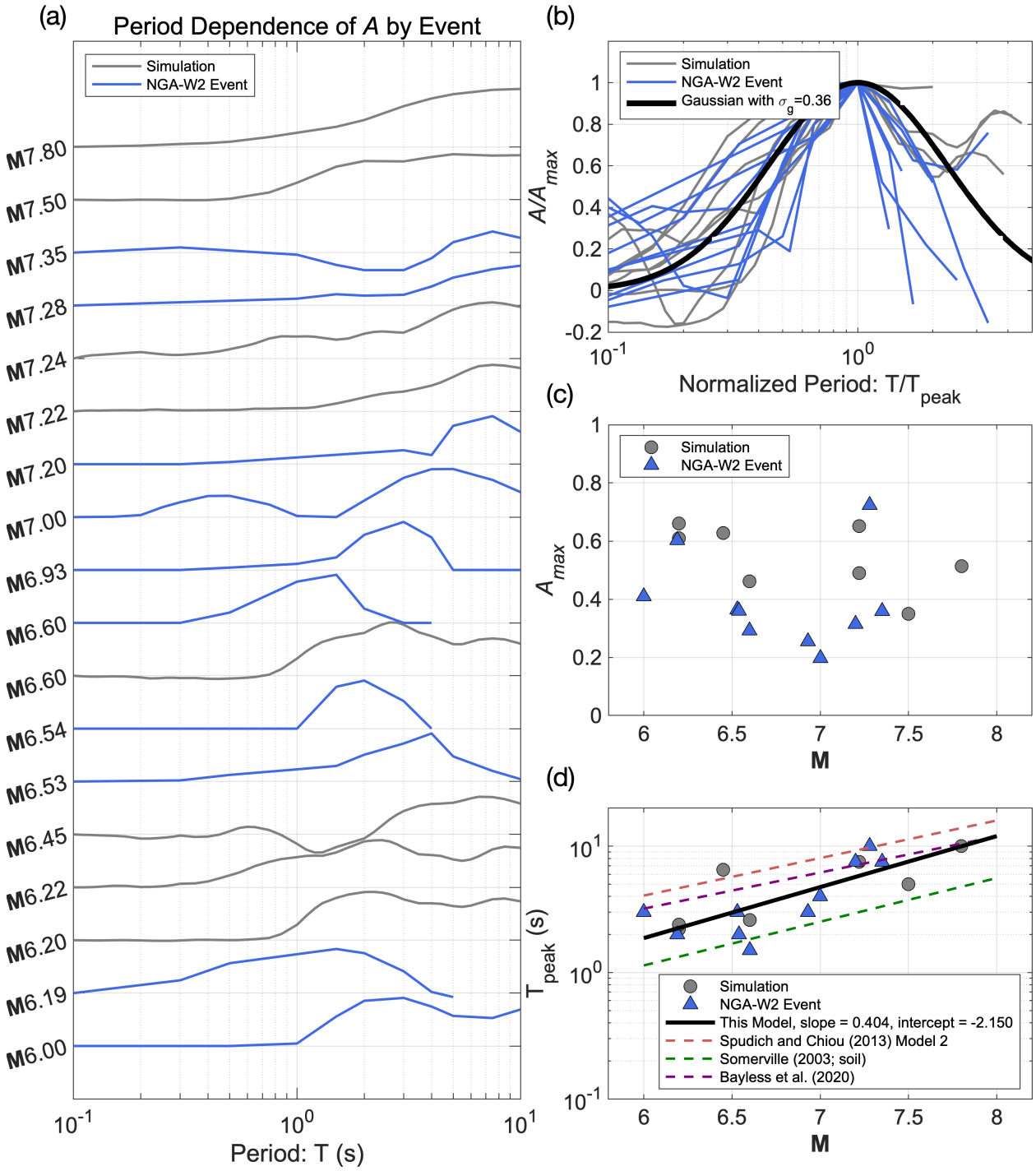


Figure C-7. Summary of Steps 3-5 for the simulated and recorded events.

# Appendix D: Aleatory Variability Model Development

Part 1: NGA-W2 Data

Using the final model coefficients, the within-event residuals of the NGA-W2 data are adjusted for median directivity effects. We calculate $\phi$ before and after this adjustment for the NGA-W2 events used to develop the median model. In these calculations, stations are included only if they are within the distance range for which the model predicts directivity adjustments (i.e. for rupture distances less than 80 km). At both stages, the within-event residuals are inspected versus rupture distance and the centered directivity predictor, $f_G'$, as shown in Figure D-1, where the red circles are the residuals after applying the directivity median adjustment. The purpose of this evaluation is to confirm that the distance scaling is not adversely affected, and to visualize the effect of the directivity model, which reduces the residuals for positive values of $f_G'$, and increases them for negative $f_G'$. In the case of the Landers earthquake (T=7.5 sec), application of the model reduces $\phi$ as indicated in the bottom panel of Figure D-1.

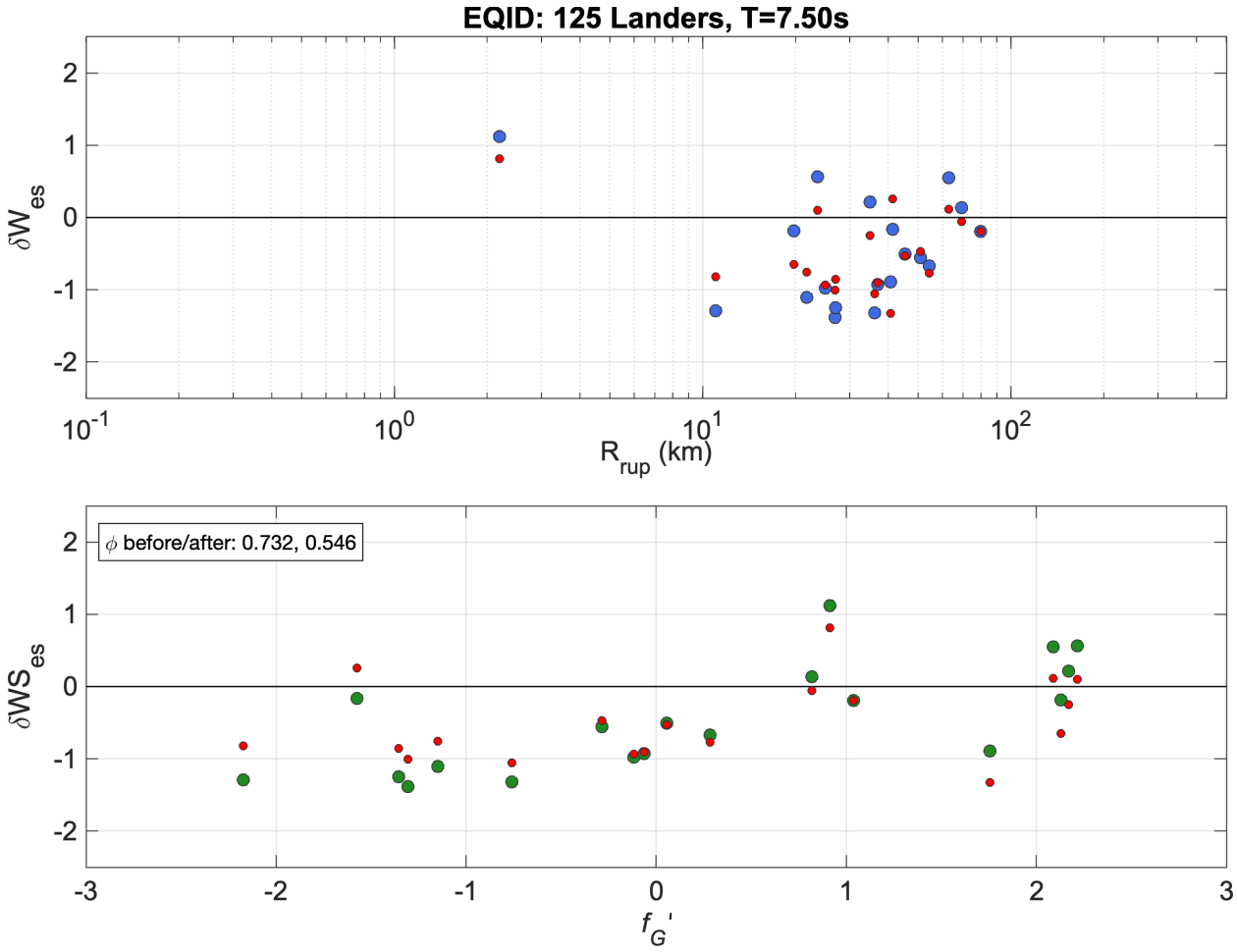


Figure D-1. The effect of applying the directivity adjustment model on Abrahamson et al. (2014) within-event residuals for the Landers earthquake, considering sites within $R_{max}$ = 80 km rupture distance, at T=7.5 sec. Blue and green circles are the residuals before the adjustment, and red circles are after.

The period dependence of $\phi_{Reduction}$ from all events is shown in Figure 4-2, and the values are listed in Table 4-3.

Part 2: Simulations

The procedure for the NGA-W2 data was followed for the simulations used to develop the median model. The period dependence of $\phi_{Reduction}$ from all simulated events is shown in Figure 4-2, and the values are listed in Table 4-3.

## Appendix E: Examples

This appendix provides a series of example applications of the model.

Example 1

This scenario (borrowed from the test scenarios in Table 1.2 of Spudich et al., 2013) is a **M**7.2 vertical strike-slip rupture with rake angle of 180 degrees, and with length of 80 km and down-dip width of 15 km. The hypocenter (red star) is located 10 km from the southern end of the rupture, at 10 km depth. The origin for the GC2 calculation required by Bea24 is the rupture surface trace ordinate of the up-dip projection of the hypocenter, which is the same as the epicenter for a vertically dipping rupture. Figure E-1 shows the spatial fields of median amplification (exponential of $f_D$) at T=3 sec spectral period, for Model 1 (simulation-based, left) and Model 2 (NGA-W2 data-based, right). The spatial patterns of amplification are the same between the models because both models have the same functional form and only differ in their coefficients.

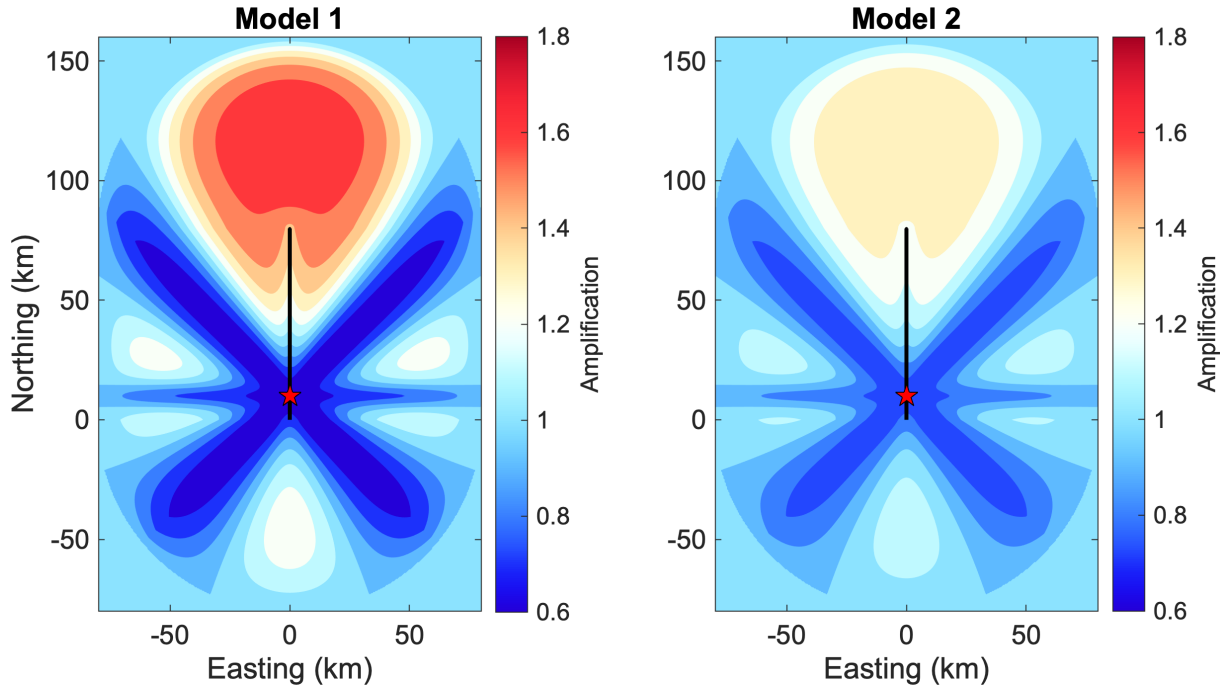


Figure E-1.The spatial fields of amplification for the Example 1 scenario rupture, T=3 sec.

Example 2

This example is based on the 2002 Denali, Alaska earthquake using the rupture model adopted by NGA-West2. This rupture model has **M**7.9 and is composed of three strands. Strand 1, which contains the hypocenter, is 45.1 km in length and 24 km width and is shallowly dipping (dip=32 deg). Strand 2 is 213.7 km long and 15 km wide, with 80-degree dip. Finally, Strand 3 is 67.9 km long and 15 km wide, with 90-degree dip. A representative rake of 171 degrees is assumed based on the larger rupture areas of strands 2 and 3 compared to strand 1. The origin for the GC2 calculation required by Bea24 is the rupture surface trace ordinate of the up-dip projection of the hypocenter (white circle). Figure E-2 shows the spatial field of Bea24 median amplification (exponential of $f_D$) at T=5 sec spectral period, for Model 1 (simulation-based, left).

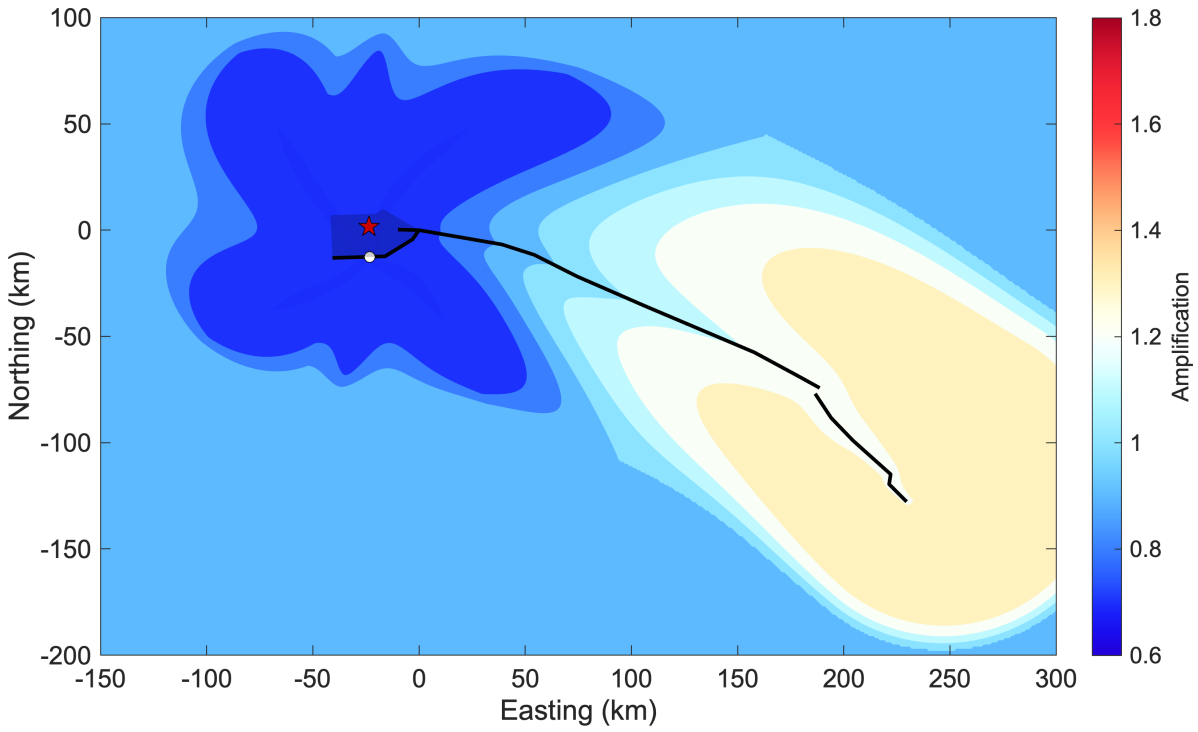


Figure E-2. The spatial fields of amplification for the Example 2 (Denali earthquake) rupture, T=5 sec.

Example 3

This example is for the **M**7.8 scenario earthquake representing the 1906 San Francisco event. The rupture is defined as in Aagaard et al., (2009). The rupture is 478 km in length and has a representative rake angle of zero degrees. Figure E-3 shows the spatial field of Bea24 (Model 1) median amplification (exponential of $f_D$) at T=7 sec spectral period.

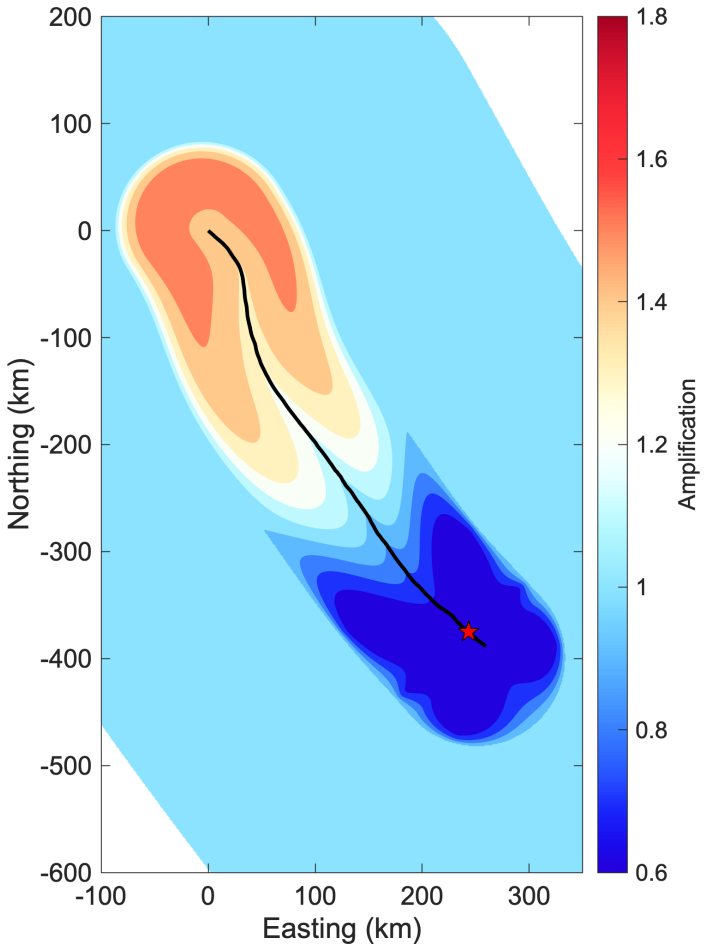


Figure E-3. The spatial fields of amplification for the Example 3 (1906 SF earthquake) rupture, T=7 sec.

Example 4

In this example, the model is applied to a hypothetical scenario earthquake. This strike-slip rupture is set up with two disconnected strands, each vertically dipping and with 22 km width. The first strand has strike of 0 degrees and 40 km length, with the hypocenter located 30 km from the southern end. The second has 45-degree strike and 28.28 km length. There is a gap of about 14 km between these strands, which is 9 km larger than the "maximum jump distance" allowed in the plausibility filters used to define UCERF3 ruptures (Field et al., 2013; Appendix T). This example demonstrates the flexibility of the model to accommodate ruptures with gaps between strands. Using the Leonard (2010) relationship for rupture area and magnitude, the scenario is prescribed **M**7.15. Figure E-4 shows the spatial field of Bea24 (Model 1) median amplification (exponential of $f_D$) at T=3 sec spectral period.

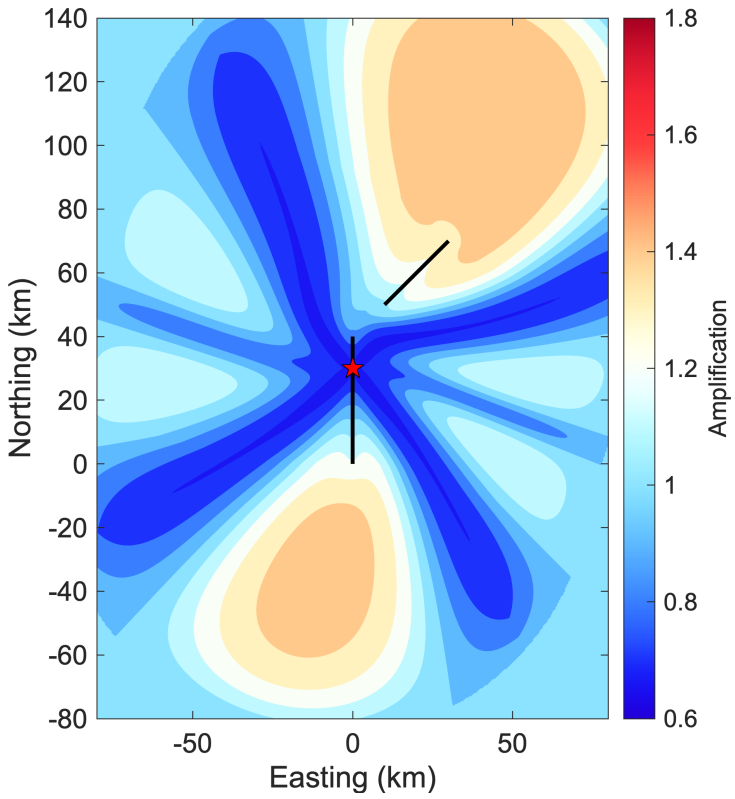


Figure E-4. The spatial fields of amplification for the Example 4 rupture, T=3 sec.

Example 5

Figure E-5 shows Bea24 (Model 1) median amplification maps for four vertical strike-slip scenarios, each north-south striking, and with hypocenter placed at the center of the rupture plane. The maps are shown at the spectral period corresponding to the scenario peak amplification ($T_{peak}$). The parameters used to define these scenarios are listed in Table E-1. With increasing magnitude, $T_{peak}$ and the maximum distance in the distance taper also increase.

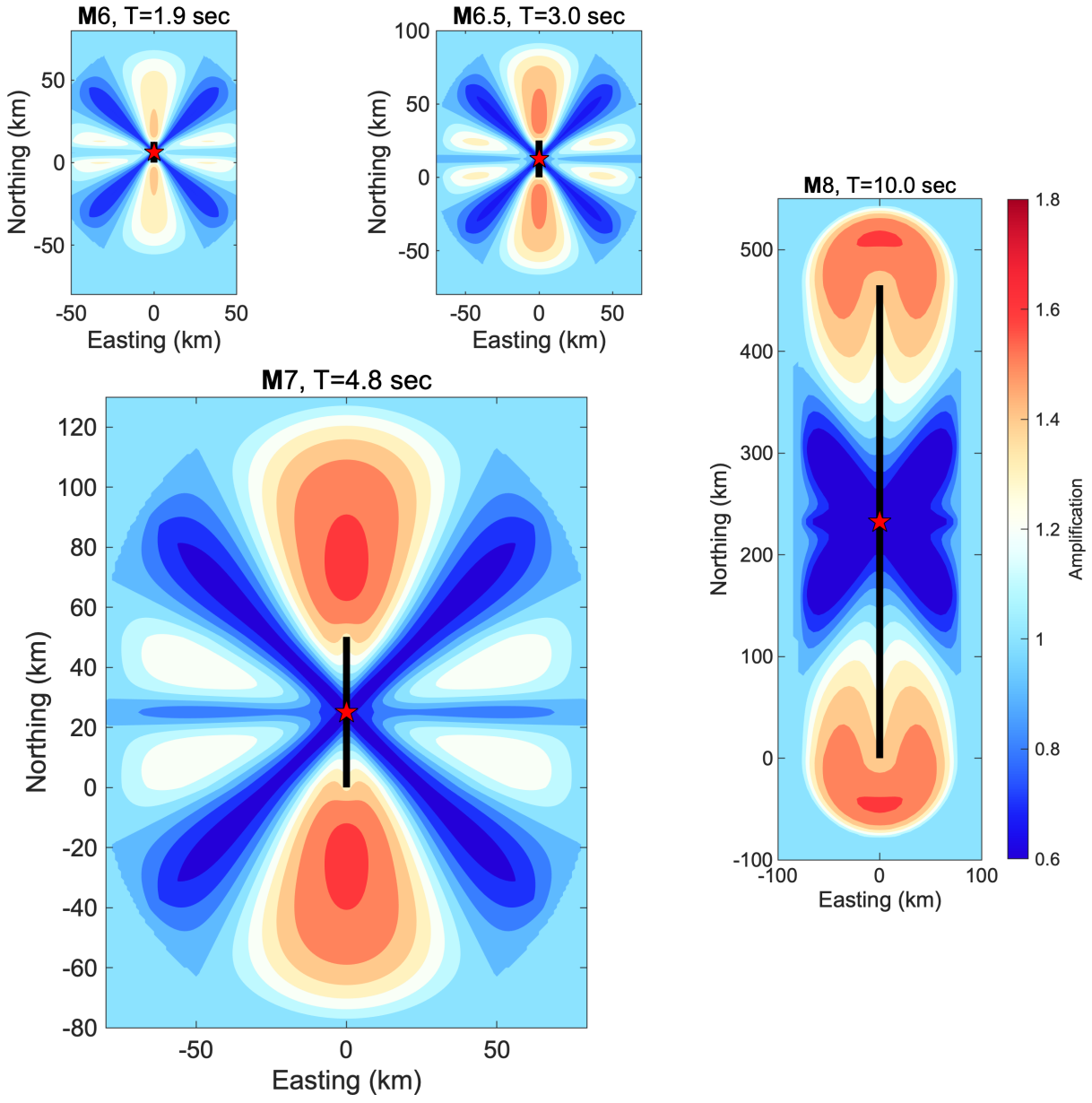


Figure E-5. The mapped median directivity adjustment (amplification) for the four strike-slip scenarios described in the text.

Table E-1. Parameters of the scenarios used to illustrate the model behavior with magnitude.

| Number | M | Length (km) | Width (km) | $T_{peak}$ (sec) |
|---|---|---|---|---|
| Strike-slip 1 | 6.0 | 12.6 | 8.12 | 1.9 |
| Strike-slip 2 | 6.5 | 25.1 | 12.8 | 3.0 |
| Strike-slip 3 | 7.0 | 50.2 | 20.4 | 6.2 |
| Strike-slip 4 | 8.0 | 465.0 | 22.0 | 10.0 |

Example 6

Figure E-6 shows T=3 sec Bea24 (Model 1) median amplification maps for four vertical strike-slip scenarios, each north-south striking and with hypocenters placed at the center of the rupture plane, with increasing $Ztor$ (0, 5, 10, and 15 km).

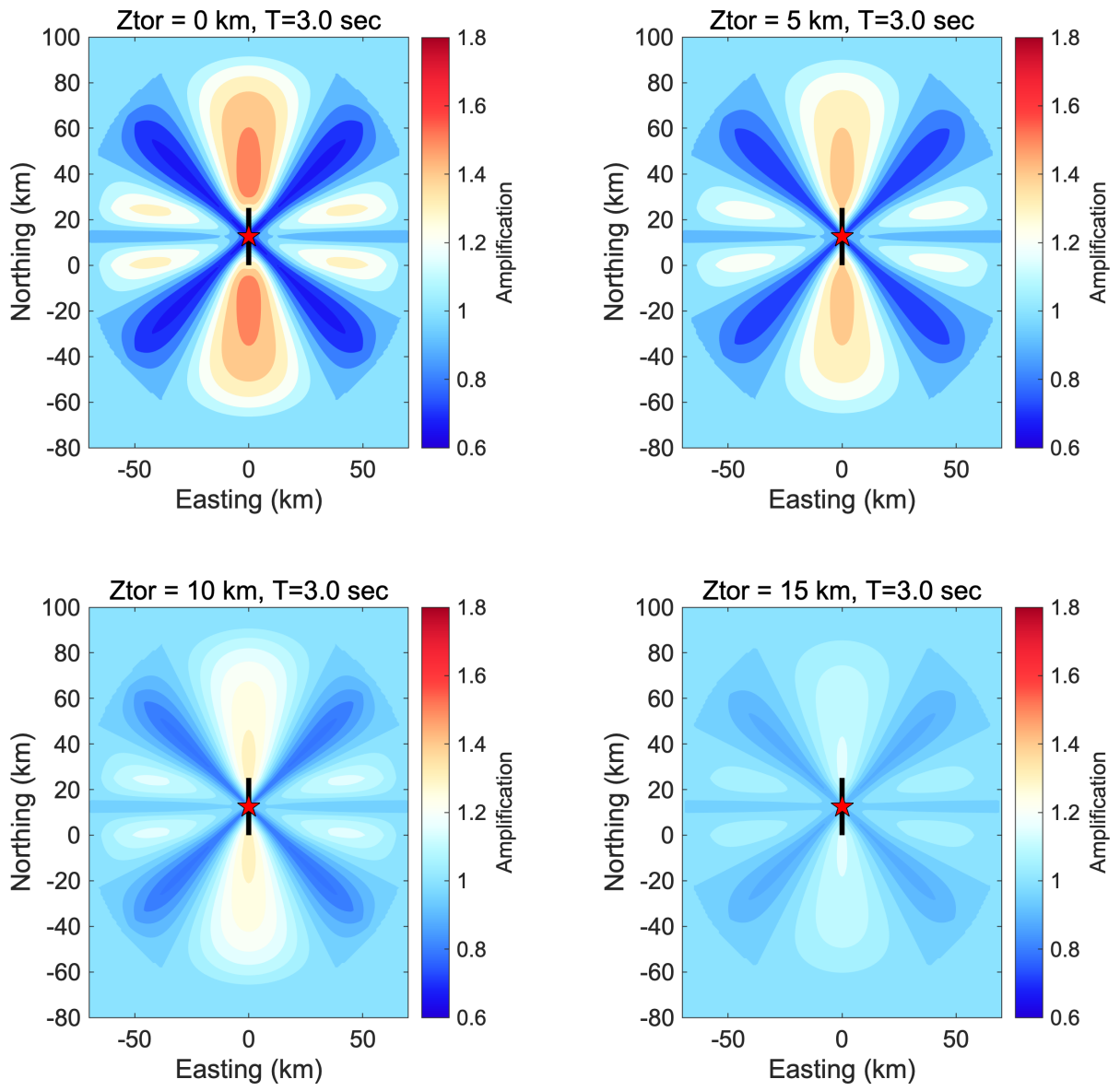


Figure E-6. The mapped median directivity adjustment (amplification) at T=3 sec for four strike-slip scenarios with increasing $Ztor$.

Example 7

This example applies Bea24 to a series of vertical strike-slip scenario earthquakes with increasing magnitude. In each scenario, the Bea24 (Model 1) is applied with unknown hypocenter locations modeled as described in Section 5.2. The Melgar and Hayes (2019) hypocenter distribution model is used to assign $P_h$ such that such that $\Sigma_k^{N_h} P_h(h_k) = 1$. The maps in Figures E-7 through E-10 show the spatial fields of $\mu_{f_D}$ and $\phi_{i|UH}$, which are calculated using Equations 8 and 9, respectively.

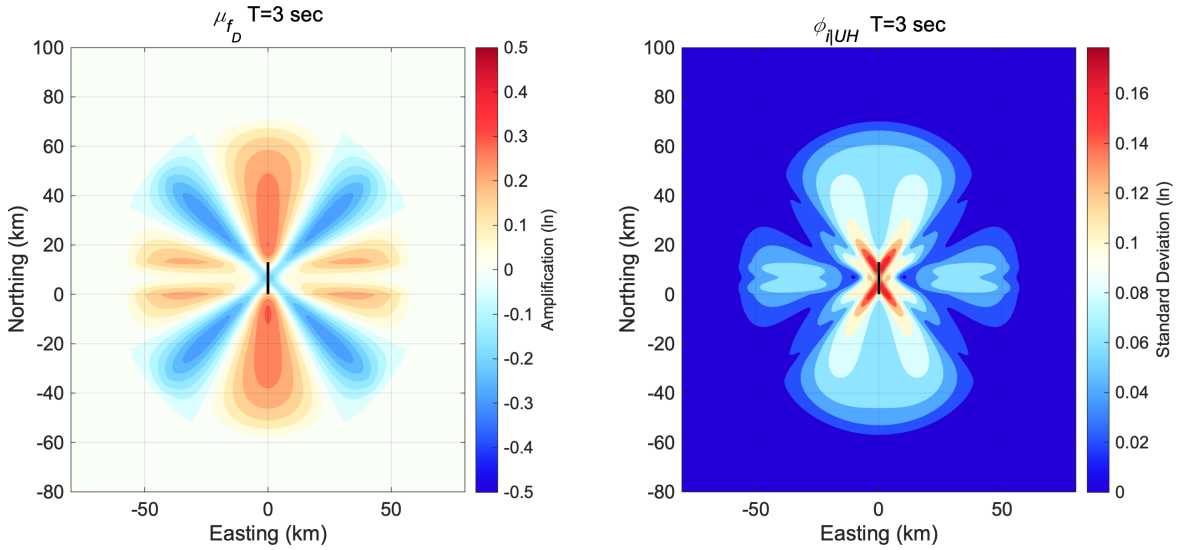


Figure E-7. Application of the Bea24 directivity model (Model 1) with unknown hypocenter location to an **M**6.0 scenario earthquake with 13 km rupture length, at 3 seconds spectral period. Left: Contours of $\mu_{f_D}$ (ln units). Right: Contours of $\phi_{i|UH}$ (ln units).

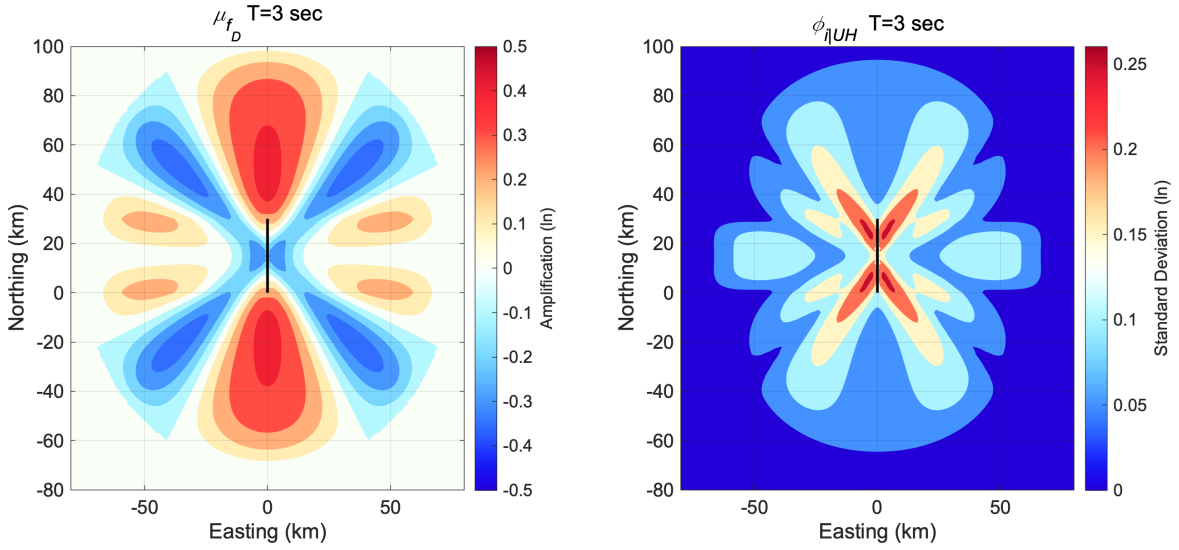


Figure E-8. Application of the Bea24 directivity model (Model 1) with unknown hypocenter location to an **M**6.6 scenario earthquake with 30 km rupture length, at 3 seconds spectral period. Left: Contours of $\mu_{f_D}$ (ln units). Right: Contours of $\phi_{i|UH}$ (ln units).

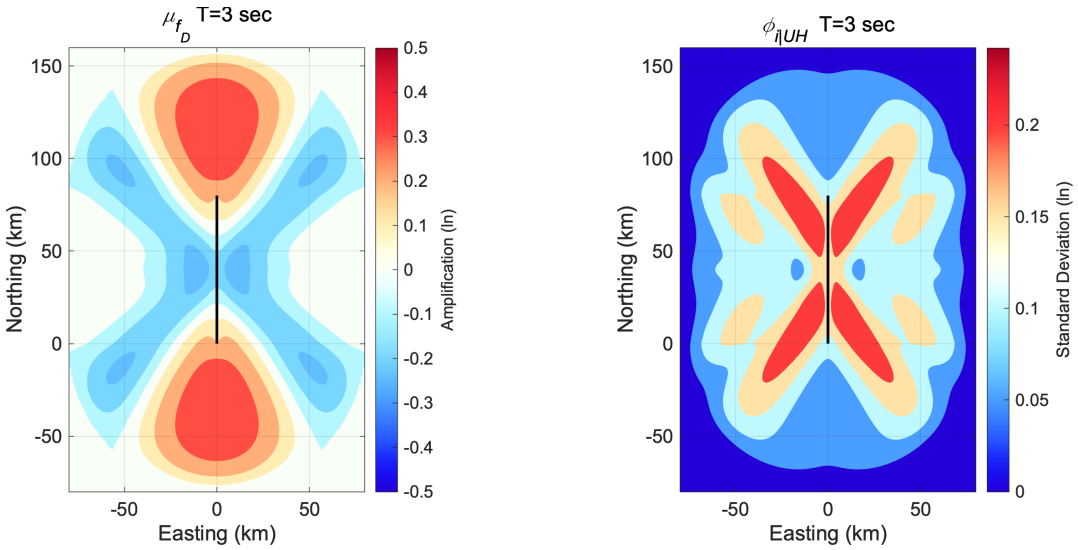


Figure E-9. Application of the Bea24 directivity model (Model 1) with unknown hypocenter location to an **M**7.2 scenario earthquake with 80 km rupture length, at 3 seconds spectral period.
Left: Contours of $\mu_{f_D}$ (ln units). Right: Contours of $\phi_{i|UH}$ (ln units).

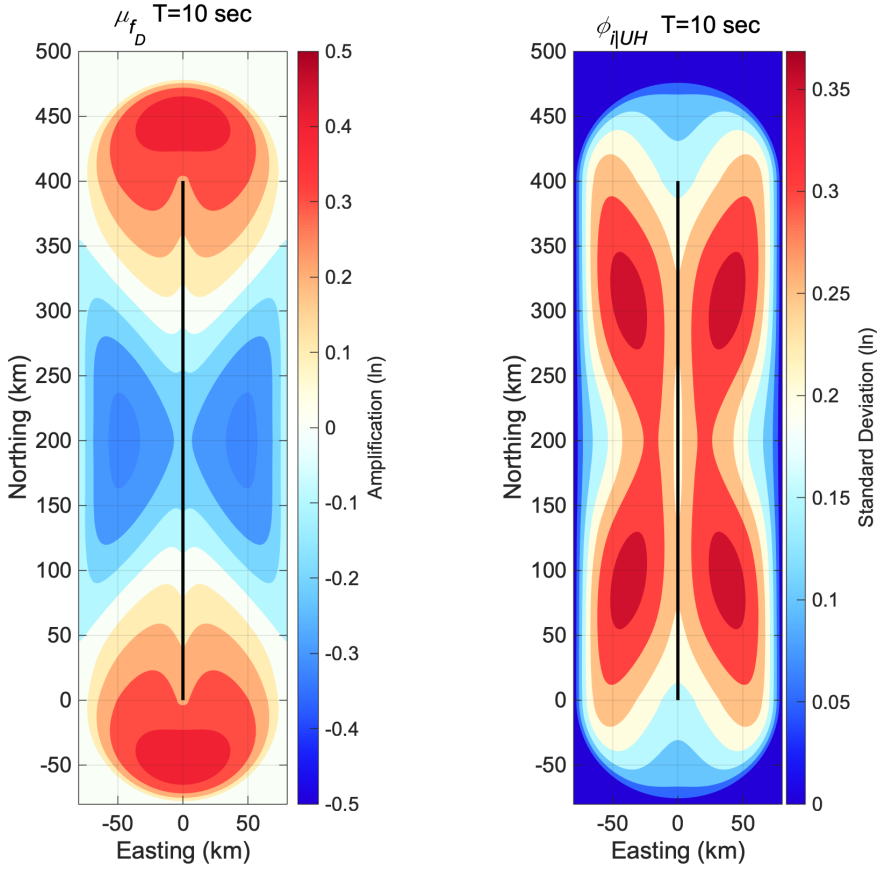


Figure E-10. Application of the Bea24 directivity model (Model 1) with unknown hypocenter location to an **M**7.8 scenario earthquake with 400 km rupture length, at 10 seconds spectral period.
Left: Contours of $\mu_{f_D}$ (ln units). Right: Contours of $\phi_{i|UH}$ (ln units).